

AD_____

Award Number: W81XWH-05-1-0396

TITLE: Angiogenic Signaling in Living Breast Tumor Models

PRINCIPAL INVESTIGATOR: Edward Brown

CONTRACTING ORGANIZATION:

University of Rochester
Rochester, NY 14642

REPORT DATE: 01^2010

TYPE OF REPORT: →

PREPARED FOR: U.S. Army Medical Research and Materiel Command
Fort Detrick, Maryland 21702-5012

DISTRIBUTION STATEMENT:

Approved for public release; distribution unlimited

The views, opinions and/or findings contained in this report are those of the author(s) and should not be construed as an official Department of the Army position, policy or decision unless so designated by other documentation.

REPORT DOCUMENTATION PAGE

Form Approved
OMB No. 0704-0188

Public reporting burden for this collection of information is estimated to average 1 hour per response, including the time for reviewing instructions, searching existing data sources, gathering and maintaining the data needed, and completing and reviewing this collection of information. Send comments regarding this burden estimate or any other aspect of this collection of information, including suggestions for reducing this burden to Department of Defense, Washington Headquarters Services, Directorate for Information Operations and Reports (0704-0188), 1215 Jefferson Davis Highway, Suite 1204, Arlington, VA 22202-4302. Respondents should be aware that notwithstanding any other provision of law, no person shall be subject to any penalty for failing to comply with a collection of information if it does not display a currently valid OMB control number. PLEASE DO NOT RETURN YOUR FORM TO THE ABOVE ADDRESS.

1. REPORT DATE (DD-MM-YYYY) 01-06-2010	2. REPORT TYPE final	3. DATES COVERED (From - To) 1 JUN 2005 - 31 MAY 2010		
4. TITLE AND SUBTITLE Angiogenic Signaling in Living Breast Tumor Models		5a. CONTRACT NUMBER		
		5b. GRANT NUMBER W81XWH-05-1-0396		
		5c. PROGRAM ELEMENT NUMBER		
6. AUTHOR(S) Edward Brown Gfy ctf aDtqy pB WTO E0Tqej guwgtQf w		5d. PROJECT NUMBER		
		5e. TASK NUMBER		
		5f. WORK UNIT NUMBER		
7. PERFORMING ORGANIZATION NAME(S) AND ADDRESS(ES) University of Rochester Â Â Rochester, NY 14642		8. PERFORMING ORGANIZATION REPORT NUMBER		
9. SPONSORING / MONITORING AGENCY NAME(S) AND ADDRESS(ES) U.S. Army Medical Research and Materiel Command Fort Detrick, MD 21702-5012		10. SPONSOR/MONITOR'S ACRONYM(S)		
		11. SPONSOR/MONITOR'S REPORT NUMBER(S)		
12. DISTRIBUTION / AVAILABILITY STATEMENT Approved for public release; distribution unlimited				
13. SUPPLEMENTARY NOTES Color Figures				
14. ABSTRACT In this grant we proposed to elucidate the signaling pathway that translates VEGFR activation into elevated vessel permeability, in endothelial cells within living breast tumor models. The working hypothesis is that the signaling pathway involved is a constitutively active form of the pathway shown for healthy mesenteric microvessels. In parallel we proposed to develop relevant optical techniques including Multiphoton Fluorescence Recovery After Photobleaching in vivo and Second Harmonic Generation (SHG) imaging. Progress to date includes the training of personnel in the laboratory, the addition to MPFRAP of the ability to measure diffusion in the presence of nearby obstacles, the elucidation of the role of the b-AR signaling pathway in breast tumor models, the elucidation of the role of PLC γ in tumor endothelial cell VEGF response, and the creation of the ability to measure the forwards/backwards scattering ratio of SHG emission from collagen.				
15. SUBJECT TERMS Angiogenesis, microscopy, signaling, VEGF, permeability				
16. SECURITY CLASSIFICATION OF: a. REPORT U		17. LIMITATION OF ABSTRACT UU	18. NUMBER OF PAGES 59	19a. NAME OF RESPONSIBLE PERSON USAMRMC
b. ABSTRACT U		19b. TELEPHONE NUMBER (include area code)		
c. THIS PAGE U				

Table of Contents

Introduction.....	4
Body.....	4
Key Research Accomplishments.....	14
Reportable Outcomes.....	15
Conclusions.....	16
References.....	N/A
Appendices.....	16

Introduction

The goals of this project are twofold: to explore signaling pathways that induce angiogenic phenotypes in endothelial cells within living breast tumor models, and to develop a series of optical techniques that contribute to this work, including second harmonic generation (SHG) imaging of breast tumor collagen, and multiphoton fluorescence recovery after photobleaching (MP-FRAP) in the presence of convective flow. This is the conclusion of the fifth (and final) year of this grant and also the fifth year of my biomedical optics laboratory here at the University of Rochester Medical Center, a laboratory which consists of myself, Dr. Kelley Madden and Dr. Seth Perry (Research Assistant Professors), Khawar Liverpool and Katie Cooley (Technicians), graduate students Javier Lapeira, Kelley Sullivan, Xiaoxing Han, and several students whose work is not funded by this award. Thanks to the Era of Hope Scholar Award we have made significant progress in our exploration of breast cancer and our development of optical techniques to advance its study. What follows is a discussion of our progress separated into four main themes

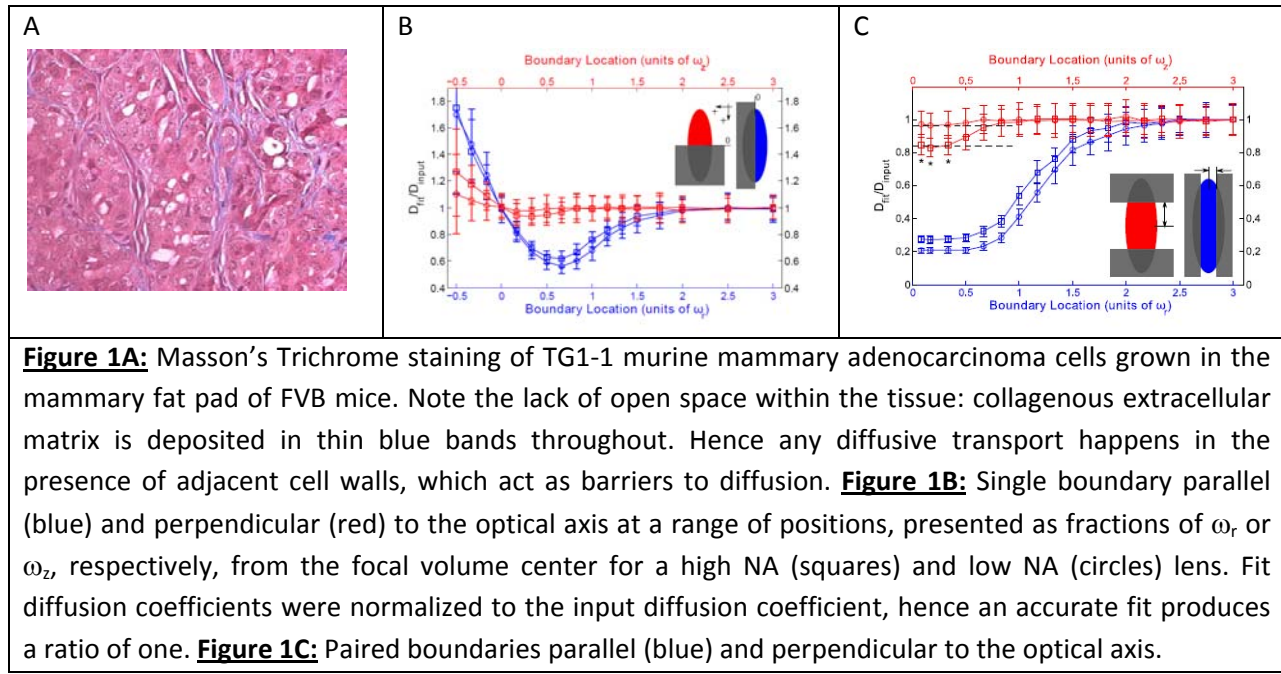
Body

1. Multiphoton Fluorescence Recovery After Photobleaching (MP-FRAP) *in vivo*.

Task 7 of the statement of work focuses on the study of convection and diffusion in the transport of macromolecules away from a breast tumor vessel. This necessitated the development of a new experimental capability: the ability to measure macromolecular diffusion with three-dimensional resolution in deep tissue. Fortunately, MP-FRAP allows for the measurement of macromolecular diffusion with 3D resolution in deep tissue, and was in fact part of my Ph.D. thesis, so we were ideally suited to extend the capabilities of this technique to allow its application *in vivo*. Over the first few years of this project, we focused on adding to MPFRAP the ability to produce accurate diffusion coefficients in the presence of convective flow. This culminated in the publication, reported last year, of Sullivan et al Biophys J 96:5082-5094 (2009). As we began to apply MPFRAP *in vivo*, however, we realized that there was another, perhaps more significant barrier to the production of accurate diffusion coefficients *in vivo*: the presence of nearby cell walls which act as barriers to diffusion. Traditional MPFRAP curves are analyzed assuming that the system is experiencing “free” diffusion, i.e. all to diffusion are at infinity and bleached molecules are free to escape the probe volume (Sullivan et al allowed for convective flow in addition to free diffusion). Some works have treated geometric constraints in the extreme limit that those constraints are close enough to change the dimensionality of the system. For example, MPFRAP performed in microvilli (thin tubes) was modeled as one-dimensional diffusion. However, there has been no analysis of the effects of barriers to diffusion when those barriers are neither at 0 nor at infinity. In the extracellular matrix of breast tumors and breast tumor models, there are always cell walls nearby (Figure 1a) and to produce accurate diffusion coefficients one must know when those walls are too close for proper curve fitting, and even better, one must have modified models of MPFRAP to fit recovery curves in the presence of those barriers.

Using Monte Carlo simulations, we have fully explored the range of barrier distances over which accurate diffusion coefficients can be generated. Figure 1b shows the results of our simulations for the

case of a single barrier at varying distances from the focal volume center, while Figure 1c shows the results of our simulations for the case of a pair of barriers centered on the focal volume. In addition we generated analytical formulae to fit the MPFRAP curves produced in the presence of these boundaries, and have significantly improved the accuracy of the resultant diffusion coefficients when single and paired barriers are placed parallel to the optical axis (Figure 2a and 2b). These geometries are directly applicable to our work in measuring interstitial transport in breast tumor models, with nearby cell walls. In addition, we modeled transport in geometries more relevant for other pursuits like neuroscience, such as MPFRAP within cylindrical and spherical boundaries (data not shown). This work was recently submitted for publication and the submitted manuscript, **Sullivan and Brown, Multiphoton Fluorescence Recovery After Photobleaching in Bounded Systems** is appended at the end of this report. Note that the graduate student who is lead author on both papers mentioned in this report, Kelley Sullivan, is my first Ph.D. student to graduate and was funded for her entire PhD on this grant.



This project has led to two useful “spin-off” projects. One is a collaboration with Dr. Mitch Anthamatten from the University of Rochester Department of Chemical Engineering. He is a polymer scientist who is interested in developing shape memory polymers, materials who substantially change their physical properties in response to changes in temperature and force. While Dr. Anthamatten is interested in these materials for their own sake, I feel that these polymers have great promise as drug delivery vehicles: they could be implanted in the location of a primary tumor resection to slowly release therapeutic agents locally, or implanted subcutaneously (as in Norplant) to slowly release anticancer or antimetastatic reagents systemically. The memory properties would then be particularly useful because reagent diffusion (and shape) properties could be greatly altered between the loading (*ex vivo*) and release (*in vivo*) steps. MP-FRAP is uniquely suitable to measure diffusion within these polymers because it can quantify diffusion with 3D resolution deep within the bulk gel, avoiding edge effects. This

collaboration culminated in the recent publication of **Li et al., Thermally activated diffusion in reversibly associating polymers** *Soft Matter* (2010) 6:235-238 and the published manuscript is reproduced at the end of this report.

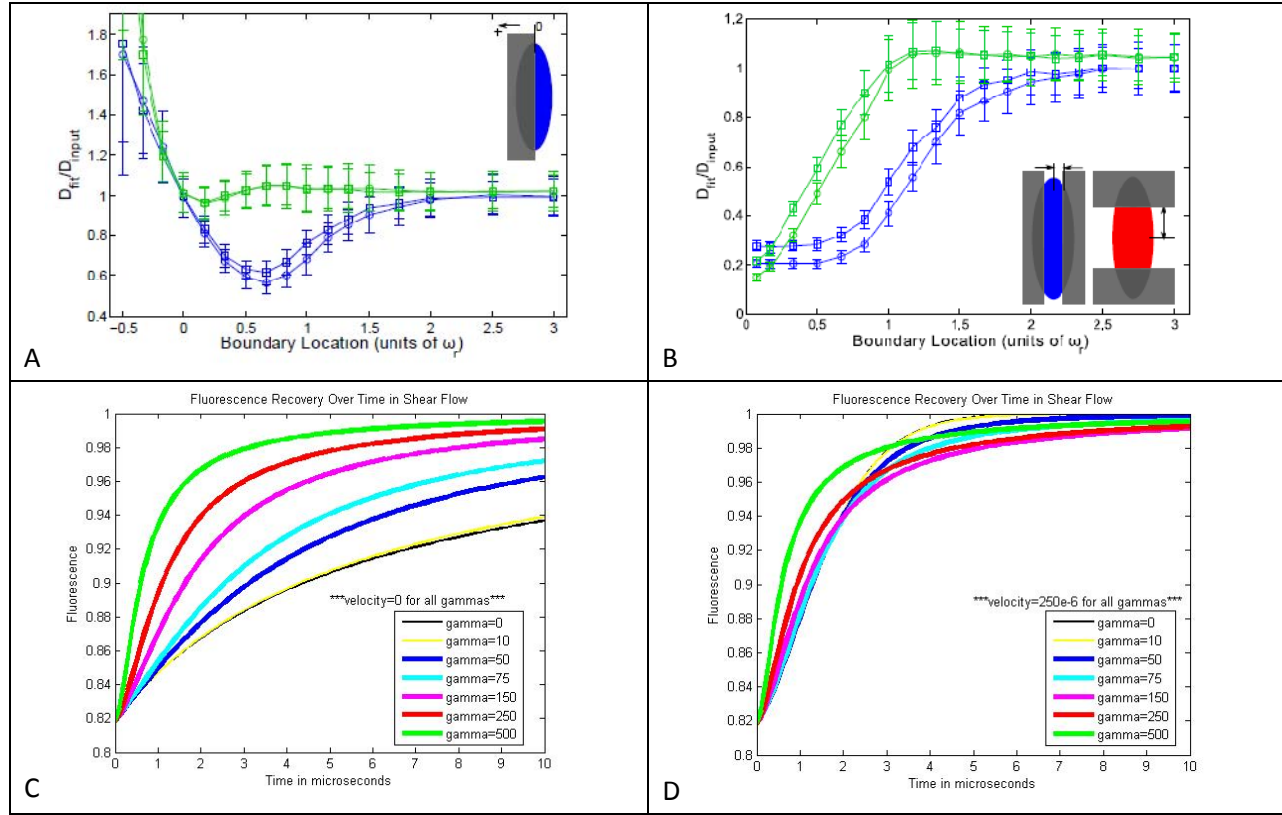


Figure 2A: The impact of the new model for fitting MPFRAP curves adjacent to a single boundary parallel to the optical axis. MPFRAP curves were simulated then fit to the classical MPFRAP model (blue) as well as the new model (green). **Figure 2B:** The impact of the new model for fitting MPFRAP curves adjacent to a pair of boundaries parallel to the optical axis. MPFRAP curves were simulated then fit to the classical MPFRAP model (blue) as well as the new model (green). **Figure 2C:** MPFRAP curves generated by the new model for fitting MPFRAP curves in the presence of shear flow, when the velocity at the center of the focal volume is zero. Each color curve represents a different shear rate gamma, with units of s^{-1} . **Figure 2D:** MPFRAP curves generated by the new model for fitting MPFRAP curves in the presence of shear flow, when the velocity at the center of the focal volume is $250\text{ }\mu\text{s}^{-1}$.

The second spinoff project is a continuation of the work we performed with Dr. Anthamatten. In the Li et al. manuscript we observed a different response to temperature between polymer diffusive hindrance and polymer viscosity. This is probably explained by the fact that the fundamental properties of the polymer are dictated by hydrogen bonds forming across polymer fibers, and by the fact that diffusion was measured by MPFRAP at equilibrium, while viscosity is measured under conditions of shear flow. In equilibrium hydrogen bonds can reform after they break, while in shear flow they cannot recombine with each other because the individual components move apart from each other after breaking. To resolve this issue we must perform MPFRAP in the presence of shear flow, i.e. $v_x(z)=v_0+\gamma z$ where v_0 is the velocity at the center of the focal volume and γ is the shear flow rate. We have

developed the mathematical model for MPFRAP in the presence of shear flow (Figure 2C,D) and have constructed a controlled shear flow device that is compatible with our microscopes. We are now testing the device in preparation for measurements of diffusion in polymers under shear flow.

2. The influence of β -adrenergic signaling on breast tumor growth and angiogenesis

Tasks 1-6 of the statement of work focus on the dissection of signaling steps leading to VEGF-induced angiogenic phenotypes in endothelial cells in tumors. As part of this work we have recently been exploring the factors upstream of VEGF, leading to its enhanced expression in the tumor microenvironment. In clinical and animal studies, exposure to emotional stressors can increase solid tumor growth, including breast cancer. The catecholamines norepinephrine (NE) and epinephrine (EPI) are important stress neurotransmitters that communicate with target cells via α - and β -adrenergic receptors (AR). NE and EPI have recently been implicated as tumor growth promoters by stimulating angiogenesis, the growth of new blood vessels into a tumor. Angiogenesis is induced by vascular endothelial growth factor (VEGF) and other proangiogenic mediators, and VEGF mRNA is upregulated in some breast tumors by β -AR stimulation. We (and others) feel that this is an exciting and underappreciated avenue to affect breast tumor growth and angiogenesis: via the influence of emotional stress on adrenergic signaling and subsequent VEGF expression. This leads to a series of questions: does β -adrenergic signaling occur in breast tumor? If so, how heterogeneous is it? What are the downstream effector molecules? And lastly, is this pathway activated by emotional stress?

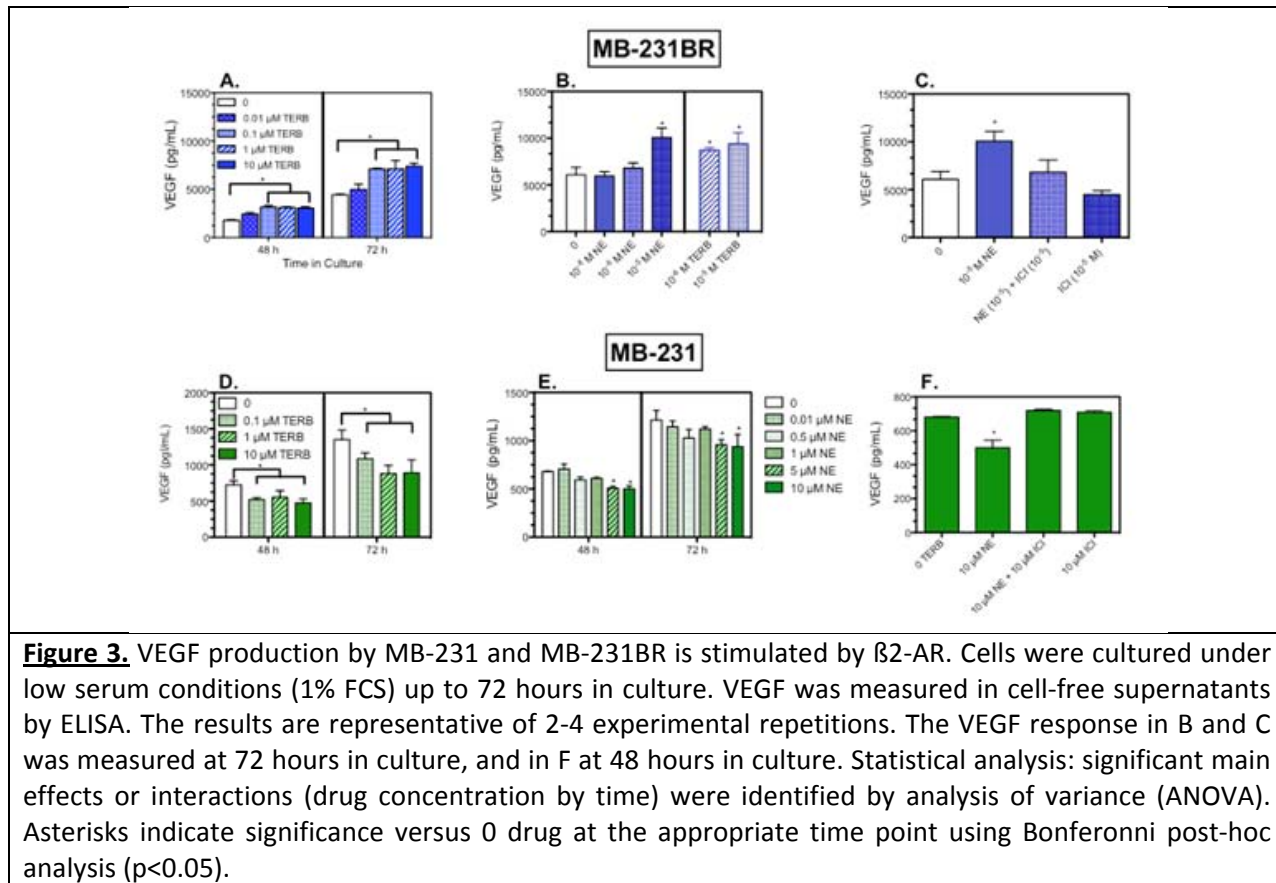


Figure 3. VEGF production by MB-231 and MB-231BR is stimulated by β 2-AR. Cells were cultured under low serum conditions (1% FCS) up to 72 hours in culture. VEGF was measured in cell-free supernatants by ELISA. The results are representative of 2-4 experimental repetitions. The VEGF response in B and C was measured at 72 hours in culture, and in F at 48 hours in culture. Statistical analysis: significant main effects or interactions (drug concentration by time) were identified by analysis of variance (ANOVA). Asterisks indicate significance versus 0 drug at the appropriate time point using Bonferroni post-hoc analysis ($p < 0.05$).

Previously we demonstrated that two human breast cancer cell lines, MB-231, a model for the aggressive ‘triple-negative’ breast cancer phenotype and its brain-homing variant, MB-231BR, express high levels of β -adrenergic receptors (β -AR). β -AR are stimulated by sympathetic nervous system release of the neurotransmitter norepinephrine (NE). We have extended our previous findings to show that NE elicits increased VEGF production by the brain homing variant MB-231BR (Fig. 3B). The magnitude of the NE-induced increase is similar to that of the β 2-AR selective agonist terbutaline (TERB) (Fig. 3A,B), and the β 2-AR selective antagonist ICI 118,551 (ICI) completely blocked the effect (Fig. 3C). These results demonstrate that the NE-induced increase in VEGF production is mediated by β 2-AR. In contrast, VEGF production by MB-231 is reduced by TERB (Fig. 3D) and by NE (Fig. 3E). The NE-induced effects were blocked by the β 2-AR selective blocker ICI 118,551 (Fig 3F), indicating that β 2-AR elicit reduced VEGF production by MB-231. Therefore, β 2-AR stimulation elicits opposite effects on VEGF production by MB-231 and MB-231BR.

To further investigate this divergent response, we next determined if β -AR activation induced a similar pattern of response for other cytokines. Constitutive production of IL-6 is detectable in both MB-231 and MB-231BR under our culture conditions. IL-6 is a multifunctional cytokine with proinflammatory and proangiogenic activities. In both MB-231 and MB-231BR, β -AR stimulation with the β 2-AR-selective agonist TERB increased IL-6 production (Fig. 4A,B).

In addition, NE increased IL-6 production in MB-231 (Fig. 4B) and the effect was completely blocked by ICI 118,551 (Fig. 4C), demonstrating that stimulation of β 2-AR increased IL-6 production in both MB-231 and MB-231BR.

To determine if the classical β -AR-adenylate cyclase-cAMP intracellular pathway was responsible for the divergent β -AR-mediated VEGF responses and β -AR-induced IL-6 production, two different pharmacological approaches were used to test the role of cAMP in regulating production of VEGF and IL-6 in MB-231 and MB-231BR. First, adenylate cyclase was directly activated with forskolin to elevate cAMP. Forskolin increased VEGF production by MB-231BR (Fig. 5A), and reduced VEGF production by MB-231 (Fig. 5C). IL-6 production was increased by forskolin in both MB-231BR (Fig. 5B) and MB-231 (Fig. 5D). These forskolin-induced alterations in VEGF and IL-6 production mimic those elicited by β -AR stimulation in both cell lines.

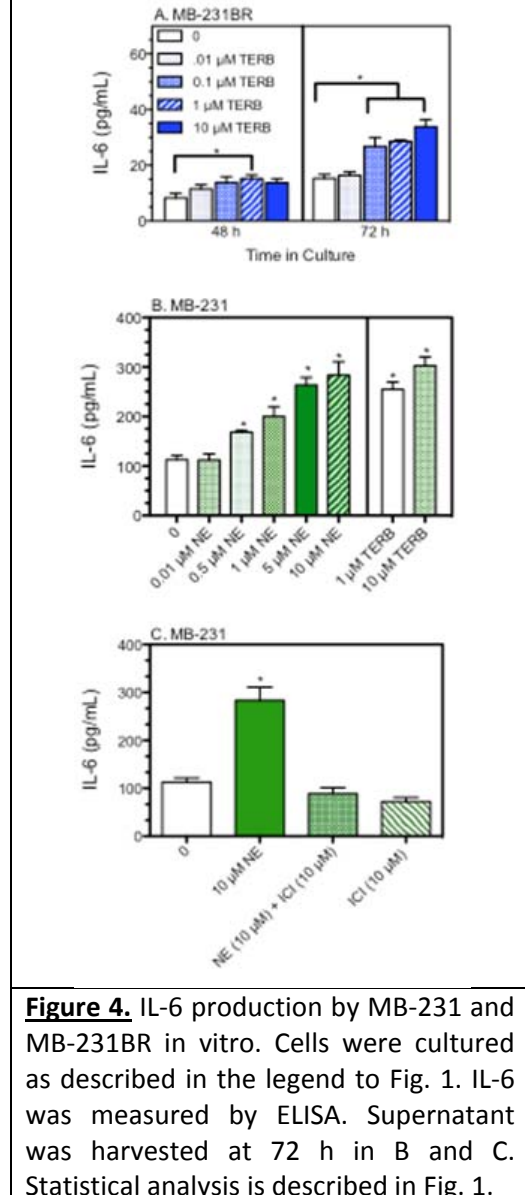


Figure 4. IL-6 production by MB-231 and MB-231BR in vitro. Cells were cultured as described in the legend to Fig. 1. IL-6 was measured by ELISA. Supernatant was harvested at 72 h in B and C. Statistical analysis is described in Fig. 1.

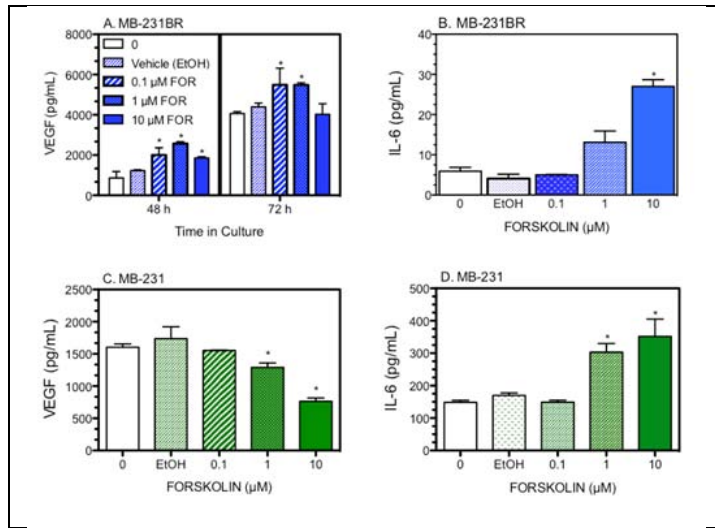


Figure 5. Forskolin-induced alterations in VEGF and IL-6 production by MB-231 and MB-231BR. Cells were cultured as described in the legend to Fig. 1. Supernatant was harvested at 72 h in B, C, and D. Statistical analysis is described in Fig. 3.

or in the presence of an optimal dose of TERB (10-6 M). In the presence of 10-8 M TERB, the effect of IBMX was significantly potentiated relative to IBMX in the absence of TERB (comparison indicated with double asterisks in Fig. 6A). Though not significant, a similar trend was detected in the presence of

rolipram. In contrast, 10-6 M TERB elicited a significant increase in VEGF production that was not further potentiated by either IBMX or rolipram (Fig. 6A). These results suggest that the impact of elevated cAMP on VEGF production is tightly controlled in MB-231BR, so that a small increase in cAMP elicited by 10-8 M TERB can potentiate the effects of IBMX or rolipram; however, the results with 10-6 M TERB suggest that cAMP-induced VEGF production reaches a maximum that is difficult to surmount by increasing cAMP concentration. This 'ceiling effect' is mostly likely mediated by inhibitory mechanisms that do not appear to be active in the context of IL-6 production.

IL-6 production in the absence of TERB was increased by the selective inhibitor rolipram, but not by IBMX (Fig. 6B). In the presence of 10-8 M TERB, which alone does not increase IL-6, the effects of IBMX and rolipram were significantly potentiated relative to IL-6 production in the absence of terbutaline (this comparison is indicated

Next, hydrolysis of cAMP by phosphodiesterases was inhibited by treatment with the cAMP phosphodiesterase inhibitor isobutyl-methylxanthine (IBMX) and the selective phosphodiesterase type IV inhibitor rolipram. This is a preliminary experiment conducted only in MB-231BR thus far. In MB-231BR, both IBMX and rolipram increased VEGF production in the absence of any other stimulation (Fig. 6A), indicating that phosphodiesterases are active even in the absence of β -AR stimulation. To determine if phosphodiesterase inhibition can further potentiate the effects of β -AR stimulation, IBMX or rolipram were incubated in the presence of a low, ineffective concentration of TERB (10-8 M)

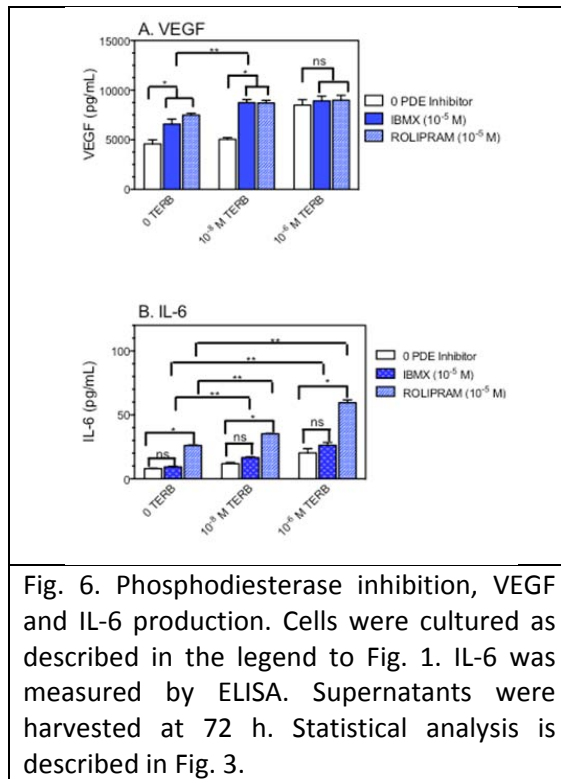


Fig. 6. Phosphodiesterase inhibition, VEGF and IL-6 production. Cells were cultured as described in the legend to Fig. 1. IL-6 was measured by ELISA. Supernatants were harvested at 72 h. Statistical analysis is described in Fig. 3.

by double asterisks in Fig. 6B). In the presence of 10-6 M TERB, phosphodiesterase inhibition further increased IL-6 production (Fig. 6B), in contrast to VEGF. At each TERB concentration, IBMX did not significantly increase IL-6 production relative to the absence of IBMX, however, the presence of TERB increased IL-6 production in the presence of IBMX relative to no IBMX. The finding that rolipram increased IL-6 production at each TERB concentration indicates that phosphodiesterase type IV plays a key role in controlling cAMP-induced IL-6 production in MB-231BR.

Together, these results suggest that cAMP is a critical effector molecule in β -AR modulation of IL-6 and VEGF production by breast cancer cells. In MB-231 and MB-231BR, cAMP potentiates IL-6 production, but it should be emphasized that these two cell lines produce detectable IL-6 under our culture conditions. In our hands, if IL-6 production by a particular cell line is undetectable, β -AR stimulation does not induce IL-6 production (data not shown). Furthermore, the cAMP pathway to IL-6 synthesis appears to lack an inhibitory component that shuts down the response to high concentrations of cAMP, unlike VEGF. (For example, compare the VEGF and IL-6 response to high concentrations of forskolin (Fig. 5) or the response to 10-6 M TERB in the presence of phosphodiesterase inhibitors (Fig. 6).) These divergent responses to β -AR stimulation and cAMP suggest that targeting breast cancer therapeutics to β -AR or cAMP pathways must be approached with care.

These results establish cAMP as a key intracellular mediator of the response to β -AR stimulation, but the regulatory intermediates that determine the qualitative response to β -AR stimulation in MB-231 and MB-231BR have yet to be determined. Studies examining the role of protein kinase A, ePAC, and other molecules downstream of cAMP in regulation of VEGF and IL-6 production are currently underway. Our original submission, listed in last year's report, on the work that precedes this was rejected with the sole substantive stipulation that the reviewers wanted more cell lines. In the process of addressing that request we also discovered the interesting behavior described above. This will now be described in two manuscripts, but those are not yet in preparation.

3. Alterations in calcium signaling in tumor endothelial cells

Our main progress on the VEGF-focused aims over the past few years has been hindered by the extremely erratic and generally poor loading of calcium indicator dyes in tumors *in vivo*. This year we decided to change the nature of the problem by attempting to take the tumor endothelial cells (TECs) *out of* the tumor, instead of trying to get the indicator dye *into* the tumor. If, as we believe, TECs are fundamentally altered by their lives within the tumor microenvironment, then we should see the same interesting contrasts between TECs and healthy ECs *in vitro* as we expected to see *in vivo*.

To produce TECs from tumors we implant 10^6 TG1-1 mammary adenocarcinoma cells in each mammary fat pad of a TIE2-GFP mouse. Hence, endothelial cells will be uniquely GFP positive. After 2 weeks of growth tumors are excised and subjected to our dissociation procedure. After many iterations of our dissociation procedure, we have produced one that generates useful numbers of TECs. It is as follows: Once the TG1-1 tumors grow subcutaneously, tumors are minced and incubated in a 0.2% solution of collagenase II, III and IV, followed by sieving the resulting cell suspension through a 70 μ m cell

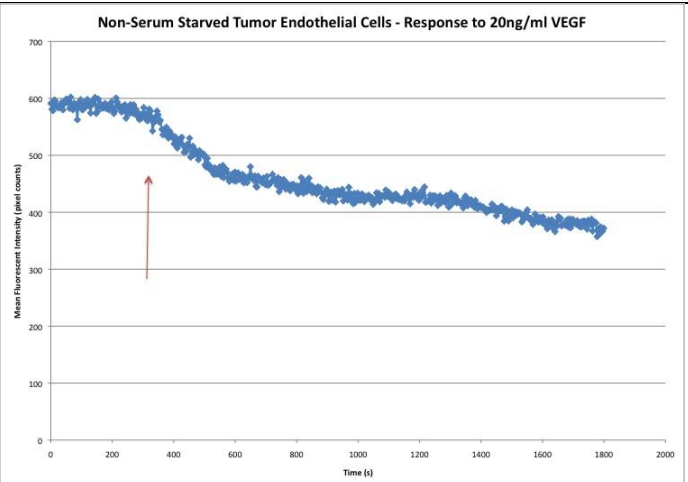
strainer. TECs are extracted using a magnetic-bead cell separation, which purifies the endothelial cell population based on the specific cell-surface marker, CD105. A biotin-conjugated CD105 antibody is used to tag the cells, after which an anti-biotin magnetic bead is used for positive selection of the TECs. For imaging, cells are plated on collagen IV-coated glass slips.

Using TECs produced by this procedure, and recognizable by their GFP fluorescence, we can now easily load them with Indo-1 indicator dye by incubating the cell culture medium with 12.4 μ M of Indo-1 AM for 45 minutes, followed by a washout step, then observe individual TECs on our MPLSM and utilize our fluid handling machinery to flow on different reagents.

Our most interesting results to-date have been obtained in non-serum starved cells, which are not subjected to 24 hours of serum starvation as is often done to enhance healthy EC response to VEGF (serum itself contains VEGF). In our non-serum starved cells, the cells reside in their growth medium (in the case of TECs they are kept in a medium containing a 3:2 ratio of basal endothelial cell medium supplemented with growth factors and TG1-1 cell conditioned medium) until 75 minutes before the experiment, at which time they are subjected to Pucks Saline solution, an isotonic solution of 0.68mM Ca^{2+} at a pH of 7.4).

We have observed that non-serum starved TECs respond to VEGF administration with an increase in intracellular calcium levels (Figure 7). This is interesting because healthy HUVECs in our hands do not respond to an increase in intracellular calcium levels when they have not been serum starved (data not shown). This suggests that the TECs VEGF/calcium handling machinery has adapted to the elevated baseline levels of VEGF in the tumor media (and maintained in serum) and can still respond to alterations in VEGF even without serum starvation.

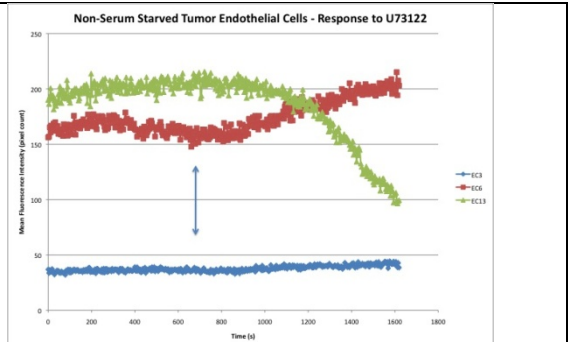
Figure 7. A representative fluorescence trace of a TEC loaded with Indo-1 AM. At the laser excitation wavelength used (760nm) Indo-1 responds to an elevation in free calcium with a decrease in fluorescence. In this case a non-serum-starved TEC (identified by its GFP fluorescence in a separate channel) responds to administration of 20 ng/ml VEGF to the medium (at the red arrow) with an increase in calcium. Non-serum-starved HUVECs do not respond in this way (data not shown).



We have also observed that non-serum starved TECs can respond to administration of U73122 (a PLC γ inhibitor) with an alteration in free calcium concentration (Figure 8). Some cells respond, as we predicted, with a decrease in cytoplasmic calcium concentration (red line in Figure 8), indicative of our hypothesized "constitutively active" calcium handling machinery. Some cells do not respond at all (blue

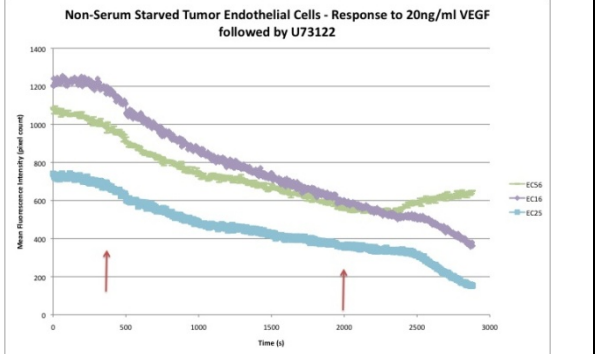
line in Figure 8), which is reasonable (and interesting!) if one believes that TECs will be highly heterogeneous and some cells may not have this constitutive activity. However, what has been most surprising is that some cells respond to administration of U73122 with an *increase* in cytoplasmic calcium concentration (green line in Figure 8). This has happened several times in several cells and warrants further investigation.

Figure 8. Representative fluorescence traces of TECs subjected to 1.12 μ M of the PLC γ inhibitor U73122 (blue line). Most cells respond with a decrease in cytoplasmic calcium (red trace) or not at all (blue trace), suggesting that a heterogeneous population of cells has constitutively active calcium handling machinery. Surprisingly, some cells respond to inhibition of PLC γ with an increase in cytoplasmic calcium (green trace).



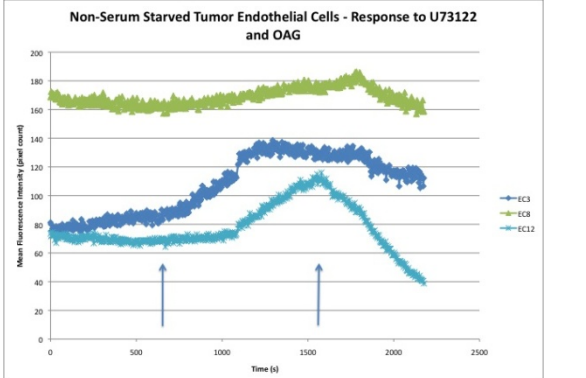
When non-serum starved TECs are subjected to 20 ng/ml VEGF followed by 2.5 μ M U73122, the majority of the cells behave as expected: calcium levels increase due to VEGF administration, and this increase is attenuated by inhibition of PLC γ with U73122 (green line in Figure 9). However, some cells again show the strange behavior whereby PLC γ inhibition further increased calcium levels, above those induced by VEGF (blue and purple line in Figure 9). Again, this contradicts our simple expectation that VEGF enhances cytoplasmic calcium levels via PLC γ activation.

Figure 9. Representative fluorescence traces of TECs loaded with Indo-1 AM and subjected to administration of 20 ng/ml VEGF (first red arrow) followed by 2.5 μ M U73122 (second red arrow). Most TECs respond to administration of VEGF with an increase in cytoplasmic calcium which is inhibited by administration U73122 (green line). However, some TECs respond with a further increase in cytoplasmic calcium (blue and purple lines).



Lastly, when non-serum starved TECs are subjected to U73122 followed by OAG (a soluble DAG analog), we see the expected decrease in cytoplasmic calcium due to U73122 inhibition of constitutively active PLC γ (although with different latency times in different cells) followed by rescue of cytoplasmic calcium with OAG, a DAG analog (Figure 10). These results support our hypothesis that calcium handling machinery in TECs is constitutively active and includes activation of PLC γ , creation of DAG, and opening of DAG-sensitive calcium channels. Note that in these limited experiments we have not encountered cells which respond to U73122 administration with an increase in calcium and have hence not observed their response to subsequent OAG administration.

Figure 10. Representative fluorescence traces of TECs loaded with Indo-1 and subjected to administration of 1.12 μ M U37122 (first blue line) followed by 100 μ M OAG, a membrane-permeant DAG analog (second blue line). All the cells studied responded to U37122 with a decrease in cytoplasmic calcium (with different latency periods) followed by a rescue of cytoplasmic calcium with OAG.



In summary, pursuit of these aims focusing on VEGF signaling has just begun to yield very interesting results, as we predicted when we started this project, however these results have been accomplished by fundamentally reworking the methods we are using to test our hypotheses. We will continue to pursue this project in the future.

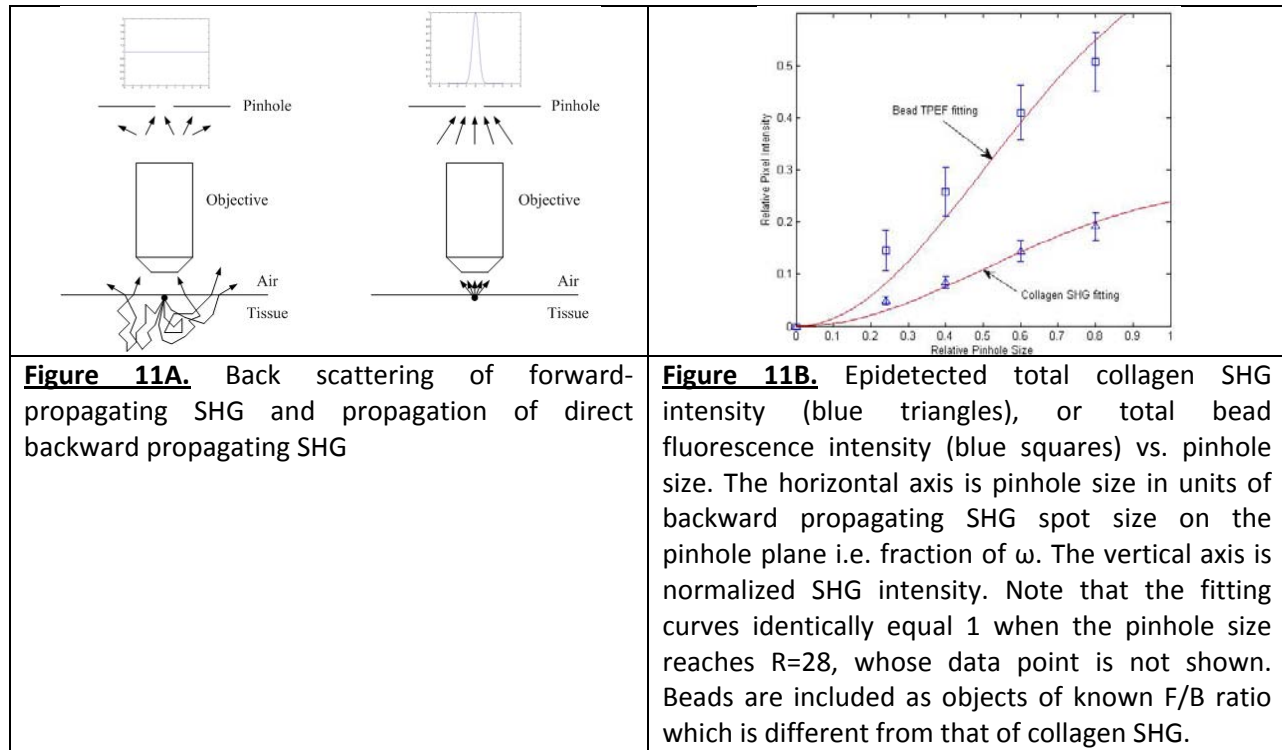
4. Second Harmonic Generation in breast tumor models.

The extremely ambitious Aim 7 of the original grant proposal led to several technological innovations in MPFRAP (discussed above) as well as in Second Harmonic Generation (SHG) imaging in breast tumor models. As reported last year this led to a “spin-off” independently funded project looking at the role of macrophages in tumor metastasis and collagen organization. One project remained funded, in part, by this grant and has now come to completion.

SHG is a coherent phenomenon, which implies that SHG is sensitive not only to the amplitude of the illumination field but also to its phase. In addition to a spatial resolution that is equal to other imaging techniques (such as two photon excited fluorescence), SHG microscopy can provide information about the sample’s molecular structure. For example, the ratio of the forward-propagating to backward propagating SHG signal (the “F/B ratio”) can help us to understand the axial extent of ordering in collagen fibers. We have recently developed a new technique to measure the F/B ratio with only one “backwards” detection objective lens, with the original intent of studying the dynamics of collagen development in mouse models of breast cancer. We have succeeded in doing this, and the paper describing our new technique has recently been published as **Han and Brown (2010) Measurement of the ratio of forward-propagating to back-propagating second harmonic signal using a single objective. Optics Express 18(8): pp.10538-10550** which is appended to this report. As I am writing to a general audience I should perhaps point out that this is the premier optics journal. This project has taken on a new urgency and excitement as a recent paper (Nadiarnykh et al 2010 BMC Cancer) has revealed that the F/B ratio of ovarian cancer is markedly different from healthy ovarian tissue. That observation, combined with our new methods, allows one to envision a wand-like “margin detection” device which would allow the surgeon to rapidly assess clinical margins in real time without the need for feedback from pathology. This would save the patient surgery time as well as reduce the number of stressful revisits after long-awaited pathology results show poor margins. Our new technique provides such a

device, which we will first explore in breast and ovarian cancer, and then branch out to other cancer types with appropriate F/B ratios.

In summary, our new technique exploits the fact that forward-propagating SHG light is diffusely scattered, and a small fraction of that light returns to the object plane as a uniform diffuse signal. If the object plane is imaged, the intensity as a function of position of that initially forward propagating light is a constant in the image plane, while the originally backward propagating light remains concentrated at the focus with a Gaussian intensity distribution in the image plane (Figure 11A). By imaging the sample through a series of 5 confocal apertures of different sizes, the relative amplitude of the Gaussian versus the constant background distribution can be determined, and the F/B ratio deduced with suitable calibration (Figure 11B).



Key Research Accomplishments in the Past Year

- 1) Completed our analysis of MPFRAP in the presence of nearby barriers, leading to a submitted manuscript.
- 2) Applied MP-FRAP to a study of polymer delivery systems, leading to a published manuscript.
- 3) Greatly extended our study of β -AR angiogenic signaling in breast tumor models.
- 4) Developed a method for extracting TECs from murine breast tumor models and studying their calcium handling machinery.
- 5) Developed a novel method for measuring SHG forward/backward scattering ratio, leading to a published manuscript.

Reportable Outcomes

Over the past year my laboratory has published four papers based upon work entirely or in part funded by this award:

Han X, Brown E (2010) Measurement of the ratio of forward-propagating to back-propagating second harmonic signal using a single objective. *Optics Express* 18(8): pp.10538-10550

Li J, Sullivan K, Brown E, Anthamatten M. (2010) Thermally activated diffusion in reversibly associating polymers. *Soft Matter* 6:235-238

Sullivan K, Brown E (2010) Measuring Diffusion Coefficients via Two-Photon Fluorescence Recovery After Photobleaching. *Journal of Visualized Experiments* (36)

Kozai T, Marzullo T, Hooi F, Langhals N, Majewska A, Brown E, Kipke D (2010) Reduction of neurovascular damage resulting from microelectrode insertion into cerebral cortex using *in vivo* two-photon mapping. *Manuscript Accepted J. Neural Eng.*

The last two manuscripts were not discussed in the body of this report. Sullivan et al 2010 is a methodological publication which helps educate the scientific community on the use of MPFRAP, while Kozai et al 2010 is an application of MPLSM to *in vivo* neurovascular imaging.

Over the past year my laboratory has contributed to the submission for publication of two additional manuscripts based upon work funded by this award:

Sullivan K, Brown E (2010) Diffusion and multi-photon fluorescence recovery after photobleaching in bounded systems. *Manuscript Submitted.*

Over the past year I have also been asked to write a book chapter, which is in preparation, while two previously prepared chapters are in press:

Han X, Perry S, Brown E. Second Harmonic Imaging of Tumors. In: Campagnola P, Pavone F (eds). *Second Harmonic Generation Imaging*. Taylor and Francis Press. *In Preparation*.

Sullivan K, Majewska A, Brown E. Single and Multiphoton Fluorescence Recovery After Photobleaching. In: Yuste R, Helmchen F, Konnerth A. (eds). *Imaging in Neuroscience and Development: A Laboratory Manual*. Cold Spring Harbor Laboratory Press, Cold Spring Harbor, New York. *In Press*.

Madden K, Zettel M, Majewska A, Brown E. Imaging Tumors in the Brain. In: Yuste R, Konnerth A. (eds). *Imaging in Neuroscience and Development: A Laboratory Manual*. Cold Spring Harbor Laboratory Press, Cold Spring Harbor, New York. *In Press*.

Over the past year I have given four invited talks based upon work funded by this award:

"Quantifying collagen organization in breast tumors using Second Harmonic Generation" Invited lecture presented at the University of Maine, 2009

"Studying the tumor extracellular matrix using nonlinear microscopy" Invited lecture presented at the Imaging Science & Technology, Rochester Chapter Meeting, Rochester, NY, 2010

"Studying cellular and molecular transport in tumors using multiphoton laser-scanning microscopy" Invited lecture presented at the University of Virginia, 2010

"Diffusion and multi-photon fluorescence recovery after photobleaching in bounded systems" Invited lecture presented at the Carl Ludwig Institute of Physiology, University of Leipzig, Leipzig, Germany, 2010

Over the past year my laboratory contributed to six poster presentations based upon work funded by this award:

Marzullo T, Kozai T, Majewska A, Brown E, Kipke D Two photon imaging of mouse neocortex vasculature combined with simultaneous multichannel recording with silicon electrode arrays Society for Neuroscience Annual Meeting, 2009

Madden K, Szpunar M, Fitzgerald K, Brown E Beta-adrenergic receptors, cAMP and Proangiogenic Factor Production by Breast Cancer Cell Lines PNIRS, 2010.

Szpunar M, Madden K, Liverpool K, Brown E Evidence for sympathetic nervous system regulation of breast cancer pathogenesis PNIRS, 2010

Szpunar M, Madden K, Liverpool K, Brown E Evidence for sympathetic nervous system regulation of breast cancer pathogenesis American Medical Women's Association, 2010 * Young Women in Science Poster Award 2nd place winner

Sullivan K, Brown E "Multi-photon fluorescence recovery after photobleaching applied to systems confined in one, two, or three dimensions." American Physical Society March Meeting. 2010.

Sullivan K, Brown E "Measuring diffusion coefficients in confined systems via multi-photon fluorescence recovery after photobleaching." Biophysical Society Annual Conference. 2010.

Conclusions

My laboratory is now finishing its fifth year of existence, and its fifth and final year of funding under this award. I feel that the significant progress my lab has made in this time has been greatly enabled by the generous support of the Era of Hope Scholar Award.

Appendix

Two papers and one manuscript are appended

Multiphoton Fluorescence Recovery After Photobleaching in Bounded Systems

Kelley D. Sullivan

*Department of Physics and Astronomy,
University of Rochester, Rochester NY 14627*

Edward B. Brown

*Department of Biomedical Engineering,
University of Rochester, Rochester NY 14627**

(Dated: July 28, 2010)

Abstract

Multi-photon fluorescence recovery after photobleaching (MP-FRAP) is a laser microscopy technique used to measure diffusion coefficients of macromolecules in biological systems. The three-dimensional resolution and superior depth penetration within scattering samples offered by MP-FRAP make it an important tool for investigating both *in vitro* and *in vivo* systems. However, biological systems frequently confine diffusion within solid barriers, and to date the effect of such barriers on the measurement of absolute diffusion coefficients via MP-FRAP has not been studied. We have used Monte Carlo simulations of diffusion and MP-FRAP to understand the effect of barriers of varying geometries and positions relative to the two-photon focal volume. Furthermore, we supply ranges of barrier positions within which MP-FRAP can confidently be employed to measure accurate diffusion coefficients. Finally, we produce two new MP-FRAP models that can produce accurate diffusion coefficients in the presence of a single or parallel infinite plane boundaries positioned parallel to the optical axis, up to the resolution limit of the multi-photon laser scanning microscope.

* Edward.Brown@urmc.rochester.edu

I. INTRODUCTION

Multiphoton fluorescence recovery after photobleaching (MP-FRAP) is a laser microscopy technique typically employed to measure diffusion coefficients within biological systems. MP-FRAP is performed by using a brief, high-intensity, laser flash to generate photobleaching within a region of interest in a fluorescent sample. The laser is then attenuated and the region of interest is monitored as still-fluorescent molecules from outside the region diffuse in to replace the outwardly diffusing bleached molecules. The resulting fluorescence *versus* time curve can be fitted to simple analytical formulae to produce the diffusion coefficient of the mobile fluorophore. In an MP-FRAP experiment, fluorescence and photobleaching are both generated via multiphoton excitation [1]. The intrinsic spatial confinement of multiphoton excitation results in a three-dimensionally resolved bleaching/monitoring volume [2], and allows MP-FRAP to measure three-dimensionally resolved diffusion coefficients within intact samples. This intrinsic spatial confinement obviates the need for a confocal pinhole and allows MP-FRAP, as well as the multiphoton laser-scanning microscope upon which it is based, to probe living tissue down to depths of several hundred microns.

Other techniques employed to measure biological diffusion include fluorescence recovery after photobleaching (FRAP), FRAP with spatial Fourier analysis (SFA-FRAP), and fluorescence correlation spectroscopy (FCS). FRAP is the precursor to MP-FRAP and was developed in the 1970's [3–5] to probe transport parameters in biological systems. However, due to the lack of spatial confinement of the one-photon excitation process, FRAP is limited to thin samples ($< 1 \mu\text{m}$) such as the plasma membrane of a cell. The use of spatial Fourier analysis allows SFA-FRAP [6] to probe diffusion in intact thick tissue, but the technique has low spatial resolution ($\sim 40 \mu\text{m}$) and is limited to the depth penetration of epifluorescence microscopy ($\sim 50 \mu\text{m}$). FCS comes in both one-photon [7, 8] and two-photon [9, 10] varieties and like MP-FRAP it can be used to measure diffusion with high, three-dimensional, resolution. FCS relies on low fluorophore concentrations (with accompanying low signals) to produce large population fluctuations within the focal volume, while FRAP relies on high fluorophore concentrations (with accompanying large signals), making the two techniques complementary, especially in the difficult optical environment of scattering tissue.

MP-FRAP has been employed to measure absolute diffusion coefficients in the cytoplasm of cells [1, 11], cartilage [12], optically fabricated gels [13], and blood plasma [14]. In these

cases, the volume surrounding the bleached spot was assumed to be “open,” with barriers to diffusion at infinity. However, many biological systems inherently confine measurements to regions within solid barriers to diffusion, such as cell walls and organelles, and to-date the effect of such barriers on the measurement of absolute diffusion coefficients via MP-FRAP has been neglected.

In the limit that these barriers become extremely close, their impact is relatively straightforward to model because they simply change the dimensionality of the system. For example, it has been shown that an MP-FRAP experiment in microvilli (an extremely narrow tube) can be modeled by one-dimensional diffusion [15, 16]. However, there has been no analysis of boundaries to diffusion positioned at intermediate distances, i.e., neither approaching zero nor at infinity, in order to determine their effects on the reported diffusion coefficient. In this work we will explore the effects of different barrier geometries on the diffusion coefficient reported by MP-FRAP, discuss the mechanism by which these barriers affect the reported diffusion coefficient, and determine the appropriate distances at which the effects of barriers can be neglected. To do this we will simulate the diffusive spread of a distribution of bleached molecules in the presence of various barriers to diffusion via Monte Carlo simulation, then calculate the resultant (two-photon) fluorescence signal, producing an artificial fluorescence *versus* time curve. We will then fit many such curves to the classical MP-FRAP equation, which assumes all barriers are at infinity, and explore how the presence of differing barriers produces errors in the reported diffusion coefficient. In the case of both a single and parallel infinite plane boundaries oriented parallel to the optical axis, we will introduce new models of MP-FRAP that explicitly account for the presence of the boundary/boundaries and explore how these new models improve the accuracy of the reported diffusion coefficients.

II. MONTE CARLO MODEL OF MP-FRAP

A. Initial fluorophore distribution

The initial concentration distribution of unbleached fluorophore immediately after the photobleaching pulse, in the limit that the boundaries to diffusion are at infinity, is given by Brown et. al [1]:

$$c(x, y, z; t = 0) = c_o \exp \left[-(1/b) q_b \delta_b \langle I_{bl}^b(x, y, z) \rangle \Delta t \right], \quad (1)$$

where c_o is the initial equilibrium concentration of fluorophore, b is the number of photons absorbed per photobleaching event, q_b is the quantum efficiency for b -photon photobleaching, δ_b is the multiphoton fluorescence action cross-section of the fluorophore for the order of excitation required for photobleaching, $\langle I_{bl}^b(x, y, z) \rangle$ is the time average of the bleach intensity raised to the b^{th} power, and Δt is the duration of the bleaching pulse.

The bleach intensity can be approximated as a 3D Gaussian [1]:

$$\langle I_{bl}^b(x, y, z) \rangle = \langle I_{bl}^b(0, 0, 0) \rangle \exp \left[-\frac{2b(x^2 + y^2)}{\omega_r^2} - \frac{2bz^2}{\omega_z^2} \right], \quad (2)$$

where ω_r and ω_z are the $1/e^2$ radial and axial dimensions of the two-photon focal volume, respectively, and $\langle I_{bl}^b(0, 0, 0) \rangle$ is the time average of the intensity at the two-photon focal volume center raised to the b^{th} power.

For the purpose of simulation, it is more efficient and effective to follow the bleached fluorophores [17–19]. Substituting Eq. 2 into Eq. 1, setting $b = 2$ for a two-photon bleaching process and $c_o = 1$ in anticipation of populating nodes later to determine the amplitude, and noting that the bleach depth parameter is defined as $\beta \equiv (1/b)q_b\delta_b\langle I_{bl}^b(0, 0, 0) \rangle\Delta t$, we find the initial distribution of *bleached* fluorophore:

$$c_{bl}(x, y, z; t = 0) = 1 - \exp \left\{ -\beta \exp \left[-\frac{4(x^2 + y^2)}{\omega_r^2} - \frac{4z^2}{\omega_z^2} \right] \right\}. \quad (3)$$

The bleach depth parameter was chosen to be $\beta = 0.25$, a value typical of experimental MP-FRAP recovery curves [1, 14]. The axial and radial extents of the focal volume were defined as $\omega_r \equiv 2.6\lambda/(2\pi\text{NA})$ and $\omega_z \equiv 8.8n\lambda/(2\pi(\text{NA})^2)$, respectively, where λ is the wavelength of the excitation laser, n is the index of refraction of the immersion medium, and NA is the numerical aperture of the lens [20]. Our simulations represent the NA extremes of typical water-immersion lenses ($\lambda = 780$ nm, $n = 1.33$, NA = 0.5 or 1.2). Space was discretized into a regular lattice with spacing defined by the expected diffusion properties (see below). One thousand bleached fluorophores were placed at lattice points using Eq. 3 as the probability distribution, and with the caveat that no fluorophores were allowed outside any diffusive barriers introduced into the system. Multiple occupancy on a single node was permitted.

B. Diffusion

Diffusion was modeled as a random walk on a three-dimensional lattice [18, 19, 21, 22]. Lattice spacing was determined by the three-dimensional diffusion equation, $\langle r^2 \rangle = 6Dt$, where the diffusion coefficient, D , was chosen *a priori* and the time step, t , was chosen to be approximately 1/1000 of the typical diffusive recovery time for a system with a diffusion coefficient D and with radial and axial focal volume widths ω_r and ω_z . For both the low- and high-NA case, D was chosen as $10\mu\text{m}^2/\text{s}$, approximately the experimental diffusion coefficient for 2000 kD fluorescein dextran [14]. The corresponding time steps were chosen as $3.12\ \mu\text{s}$ and $0.376\ \mu\text{s}$, respectively, and the lattice spacing was calculated to be 13.7 nm and 4.75 nm, respectively.

C. Boundary conditions

Four boundary models were applied to the diffusing system: a single infinite-plane boundary parallel and perpendicular to the optical axis, two infinite parallel-plane boundaries parallel and perpendicular to the optical axis, a hollow infinite-cylinder boundary parallel and perpendicular to the optical axis, and a hollow spherical boundary. In the context of our simulations a barrier is considered infinite if a particle cannot cross the barrier at any time during the simulation. The parallel, cylindrical and spherical boundaries were positioned symmetrically about the focal volume center, and the positions of all of the boundaries were defined as fractions of ω_r or ω_z relative to the focal volume center. All boundaries were assumed to be perfectly reflecting, i.e., any particle attempting to cross a boundary was returned to the node it was occupying when the step began. There were no bleached or unbleached molecules beyond the boundaries at $t = 0$, or at any subsequent point.

D. MP-FRAP

The fluorescence intensity generated by a weak monitoring beam through an m -photon process is given by:

$$F(t) = \frac{\delta_m E}{m} \int \langle I_{mo}^m(x, y, z) \rangle c(x, y, z; t) dx dy dz, \quad (4)$$

where δ_m is the multiphoton fluorescence action cross-section of the fluorophore for the order of excitation required to produce fluorescence, E is the collective efficiency of the detection system, and m is the number of photons absorbed per excitation event.

We can calculate the fluorescence that would be generated by the bleached fluorophores were they *not* bleached by re-expressing the integral as a sum over all bleached fluorophore locations (x_i, y_i, z_i) . We can also let $(1/m)E\delta_m \rightarrow 1$, as it will be divided out when the fluorescence is normalized for fitting:

$$F_{bl}(t) = \sum_i \exp \left[-\frac{2b(x_i^2 + y_i^2)}{\omega_r^2} - \frac{2bz_i^2}{\omega_z^2} \right]. \quad (5)$$

To obtain the fluorescence of the *unbleached* molecules, we first normalize the “fluorescence” of the bleached molecules by the pre-bleach fluorescence, F_o , and then subtract from one: $F(t)/F_o = 1 - F_{bl}(t)/F_o$. F_o was determined by first setting $t = 0$ and $\beta = 0.25$ in Eq. 6, below, truncating the sum to the first ten terms, and solving for $F(0)/F_o$. This value was then substituted into $F(0)/F_o = 1 - F_{bl}(0)/F_o$ to deduce F_o from $F_{bl}(0)$.

The natural variation of a Monte Carlo simulated random walk introduced a small amount of noise into the resulting $F(t)$ recovery curves. On top of this, we added Poisson distributed noise to mimic the typical distribution of noise arising from photon counting experiments, and in an amount typical of *in vitro* MP-FRAP experiments [1, 14]. Fluorescence recoveries were terminated when the change in the recovered fluorescence was less than 1% over a time equivalent to the half-time for complete recovery of a freely diffusing system with diffusion coefficient D .

Unless otherwise stated, all simulated $F(t)$ curves were fit to the accepted diffusive recovery model [1]:

$$\frac{F(t)}{F_o} = \sum_{n=0}^{\infty} \frac{(-\beta)^n}{n!} \frac{1}{(1 + n + 2nt/\tau_D)} \frac{1}{(1 + n + 2nt/R\tau_D)^{1/2}}, \quad (6)$$

where τ_D is the characteristic diffusion time and R is the square of the ratio of the axial and radial dimensions of the focal volume. The diffusion coefficient is given by $D = \omega_r^2/8\tau_D$.

III. RESULTS AND DISCUSSION

A. Single plane boundary

We begin our Monte Carlo investigation by introducing a single infinite-plane reflective boundary parallel to the optical axis, at a range of distances measured in units of ω_r relative to the focal volume center. This models diffusion measurements adjacent to cell walls [23–25]. We then generate an initial distribution of bleached molecules according to Eq. 1, with the caveat that no molecules are located beyond the boundary. Then we simulate the random diffusion of those molecules and produce an $F(t)$ curve as described above. The resultant curve is fit to Eq. 6, the MP-FRAP formula that assumes all boundaries are at infinity. The fit (possibly erroneous) diffusion coefficient is then divided by the true diffusion coefficient (defined *a priori* in setting up the diffusion random walk), hence errors due to the presence of a boundary are readily identified by a deviation of this ratio from one. Note that we ceased our simulations at a boundary location of $-0.5\omega_r$ because at this point the average fluorescence from the focal volume in steady state is $< 10\%$ of the value of the unobstructed focal volume.

The resultant data is presented in Fig. 1, and shows that MP-FRAP begins to yield diffusion coefficients significantly different from the input diffusion coefficient (defined hereafter as when the mean fit diffusion coefficient is more than one standard deviation different from the input diffusion coefficient) when the boundary passes a distance of $1.3\omega_r$ from the focal volume center for a high NA lens and $1.5\omega_r$ for a low NA lens. In each of these cases, the fit diffusion coefficient, D , becomes significantly different from the input coefficient before the boundary crosses the focal volume center ($0\omega_r$), and the deviation is biphasic, with an initial underestimation of the diffusion coefficient becoming an overestimation as the boundary crosses the focal volume center. The underestimation of D is most pronounced when the boundary is in the range of $\sim 0 - 1.5\omega_r$, and we hypothesized that this occurs because the boundary hinders the complete escape of bleached molecules from the focal volume, forcing a selection of fluorophores to reside longer in the neighborhood of the focal volume, thereby lengthening the recovery time. We further hypothesized that as a growing portion of the focal volume becomes “hidden” behind the boundary its characteristic radial size will become smaller than ω_r and fitting of the resultant recovery curves to Eq. 6, which assumes

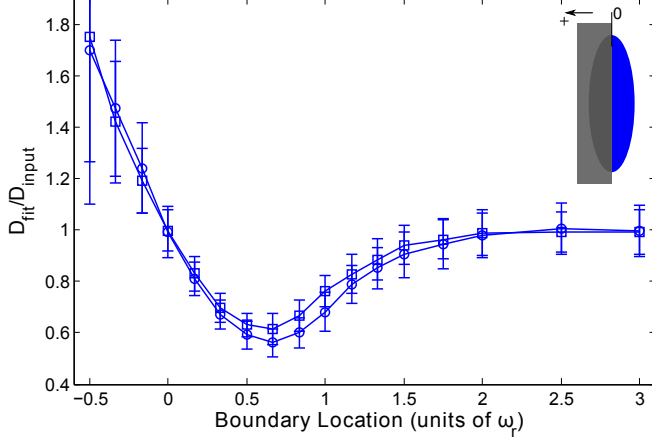


FIG. 1. Single boundary parallel the optical axis at a range of positions, presented as fractions of ω_r from the focal volume center, for both a high NA (squares) and low NA (circles) lens. Negative position values indicate that the boundary has crossed the focal volume center (i.e., more than half the focal volume is hidden beyond the boundary). Fluorescence recovery curves were generated via Monte Carlo simulation and fit to the standard MP-FRAP model Eq. 6. Fit diffusion coefficients were normalized to the input diffusion coefficient, hence an accurate fit produces a ratio of one.

that ω_r is the relevant radial length scale, will produce the growing overestimation of D that becomes apparent as the wall approaches $-0.5\omega_r$.

To test these hypotheses we first repeated the series of Monte Carlo simulations, now using a “destructive” boundary instead of a “reflective” one, such that each bleached molecule that attempted to cross the boundary was removed from the simulation. As shown in Fig. 2, removal of the reflected fluorophores eliminated the initial underestimate in D but retained the later overestimate, suggesting that it is indeed reflection of bleached molecules off of the boundary and back into the focal volume that lengthens the recovery time and leads to the initial underestimate of D . One may note that the curves describing the destructive case begin to upswing while those for the reflective case are still in their initial downturn. At this point in the reflective case the effect on recovery is dominated by the fluorophores reflecting back into the region of the focal center, and only as the boundary crosses the focal center does the effect on shortening ω_r begin to overcome particle deflection and reverse the trend, eventually leading to overestimates of D .

Next, to demonstrate the effect that changing the focal volume dimensions has on fluo-

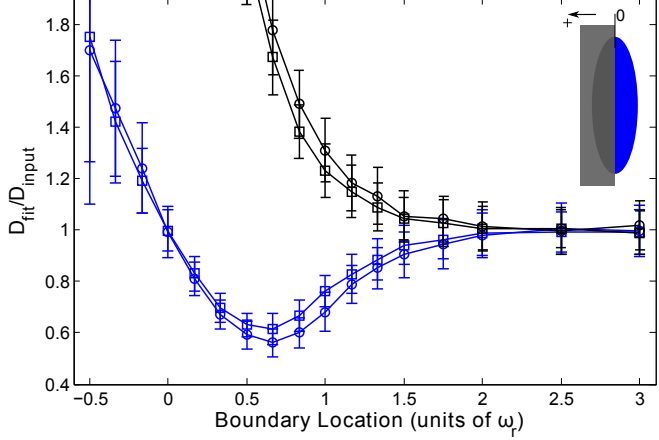


FIG. 2. Single “destructive” boundary (black) and “reflective” boundary (blue) parallel to the optical axis at a range of positions, presented as fractions of ω_r from the focal volume center for a high NA (squares) and low NA (circles) lens. Negative position values indicate that the boundary has crossed the focal volume center (i. e. more than half the focal volume is hidden beyond the boundary). Fluorescence recovery curves were generated via Monte Carlo simulation and fit to the standard MP-FRAP model. Fit diffusion coefficients were normalized to the input diffusion coefficient, hence an accurate fit produces a ratio of one.

rescence recovery and fitting, we generated data assuming an unobstructed focal volume and free diffusion, but with ω_r reduced to mimic the influence of the barriers reducing the focal volume as introduced in the previous simulations. We then fit the resulting fluorescence curves assuming a focal volume with the original ω_r . As ω_r was reduced to successively smaller values, the fit diffusion coefficient was increasingly overestimated (data not shown). This reproduces the trend seen in Fig. 2 and suggests that the overestimate in D is indeed due solely to a reduction in the bleaching distribution and monitoring volume, and hence an overestimate of their characteristic size during the fitting process.

Inspection of Fig. 1 also reveals that the low NA curve is more affected by the approach of the barrier than is the high NA curve, with a more significant initial underestimate of D . We hypothesized that this is due to the different aspect ratios of the focal volumes ($\omega_z/\omega_r = 3.75$ for the high NA case and $\omega_z/\omega_r = 9$ for the low NA case). The fastest route for diffusive escape from an initial bleached distribution will be along the shortest dimension of the initial distribution, and the higher aspect ratio of the low NA focal volume

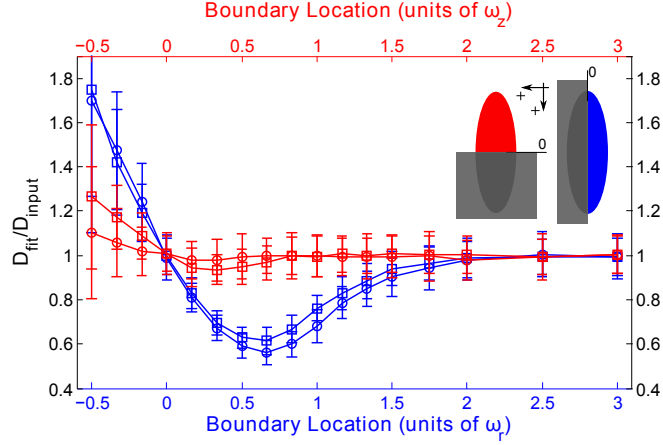


FIG. 3. Single boundary parallel (blue) and perpendicular (red) to the optical axis at a range of positions, presented as fractions of ω_r or ω_z , respectively, from the focal volume center for a high NA (squares) and low NA (circles) lens. Negative position values indicate that the boundary has crossed the focal volume center (i.e., more than half the focal volume is hidden beyond the boundary). Fluorescence recovery curves were generated via Monte Carlo simulation and fit to the standard MP-FRAP model. Fit diffusion coefficients were normalized to the input diffusion coefficient, hence an accurate fit produces a ratio of one.

means that the diffusive transport in the direction of the approaching barrier is a more significant contributor to fluorescence recovery for that objective lens than for a higher NA objective, resulting in a more significant effect of the barrier. To test this hypothesis we repeated the series of Monte Carlo simulations, but brought in a barrier to diffusion that was perpendicular to the optical axis. The fastest route for diffusive escape in this geometry is now parallel to the surface of the approaching barrier and thus unhindered by it, leading us to predict that the initial underestimate of D should be greatly reduced. Furthermore, the underestimate of D should now be *least* significant for the low NA case, as that has the highest aspect ratio. As shown in Fig. 3, the initial underestimate of D for the boundary perpendicular to the optical axis is indeed greatly reduced, and is now least significant for the low NA case, thus confirming our hypothesis. Fig. 3 also reveals that MP-FRAP begins to yield diffusion coefficients significantly different from the input diffusion when a boundary perpendicular to the optical axis passes $-0.3\omega_z$ for a high NA lens. For the low NA case, the fit diffusion does not deviate significantly for any of the boundary locations assessed.

To improve the accuracy of the reported diffusion coefficient for the case of a single barrier to diffusion, we have derived an alternative analytical model of the fluorescence recovery (see Appendix) that takes into account the presence of the barrier. For a barrier lying parallel to the optical axis, the new model is:

$$\frac{F(t)}{F'_o} = \frac{1}{2} \frac{1}{\text{erfc}(-2u/\omega_r)} \sum_{n=0}^{\infty} \frac{(-\beta)^n}{n!} \frac{1}{(n + \mu_n(t))} \frac{1}{(n + \nu_n(t))^{1/2}} \\ \times \left\{ \text{erfc} \left[-2(1 + n/\mu_n(t))^{1/2} \frac{u}{\omega_r} \right] + \exp \left[-\frac{16n}{n + \mu_n(t)} \left(\frac{u}{\omega_r} \right)^2 \right] \text{erfc} \left[-2 \frac{(1 - n/\mu_n(t))}{(1 + n/\mu_n(t))^{1/2}} \frac{u}{\omega_r} \right] \right\}, \quad (7)$$

where $\mu_n(t) = 1 + 2nt/\tau_D$, $\nu_n(t) = 1 + 2nt/R\tau_D$, and u is the x or y position of the bleached molecule distribution center relative to the boundary. For a barrier perpendicular to the optical axis, the form is the same but $\mu_n \rightarrow \nu_n$ and $\omega_r \rightarrow \omega_z$ in the exponential and complementary error functions.

When the new MP-FRAP “single boundary” model is used to fit simulated diffusion curves produced in the presence of a single barrier parallel to the optical axis, the reported diffusion coefficients improve dramatically over a wide range of barrier distances (see Fig. 4). For the case of a barrier perpendicular to the optical axis the reported diffusion coefficients do not improve significantly over the already generally accurate results using the standard model (data not shown). Fig. 4 shows that the fit diffusion coefficient remains accurate until after the boundary has crossed the center of the focal volume ($0\omega_r$), assuming the position of the focal volume with respect to the boundary (u) is known. The fit diffusion coefficient becomes significantly different from the input diffusion coefficient as a boundary parallel to the optical axis passes $-0.15\omega_r$ from the focal volume center for both a high and low NA lens. If the position of the boundary is not known (i.e., beyond the resolution limit of the multi-photon laser scanning microscope), we can allow u to be a free fitting parameter. However, doing so yields erroneous values for the diffusion coefficient for sub-resolution barrier positions (data not shown).

From these simulations we have determined that when an MP-FRAP experiment is performed adjacent to a single plane barrier to diffusion, and the fluorescence recovery curves are fit to the standard MP-FRAP model, erroneous diffusion coefficients can be produced which trend from underestimates of D to overestimates of D as the barrier approaches and passes the center of the focal volume. This is caused by a hindrance of the ability of bleached

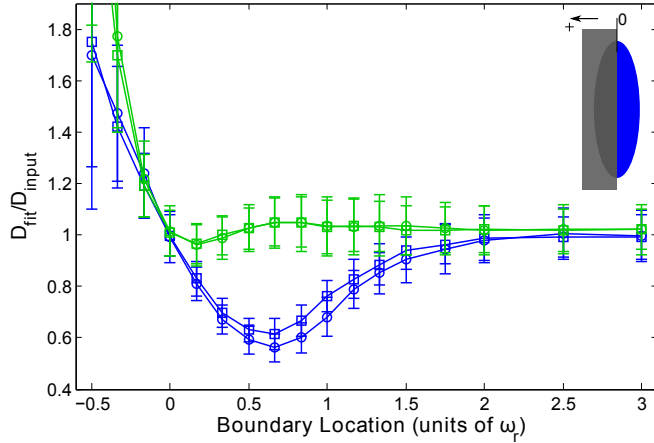


FIG. 4. Single boundary parallel to the optical axis at a range of positions, presented as fractions of ω_r from the focal volume center for a high NA (squares) and low NA (circles) lens. Negative position values indicate that the boundary has crossed the focal volume center (i.e., more than half the focal volume is hidden beyond the boundary). Fluorescence recovery curves were generated via Monte Carlo simulation and fit to the standard MP-FRAP model (blue) and the new MP-FRAP model (green) designed for use near a single barrier. Fit diffusion coefficients were normalized to the input diffusion coefficient, hence an accurate fit produces a ratio of one.

molecules to leave the environment of the focal volume, coupled with a truncation of the bleach distribution and monitor volume. Using the standard MP-FRAP model, the onset of these deviations is at a distance of $1.3 - 1.5\omega_r$ for a barrier parallel to the optical axis and $\sim -0.3\omega_z$ for a barrier perpendicular to the optical axis. Due to the high aspect ratio of two-photon focal volumes, the underestimate is most significant when the barrier is parallel to the optical axis. Using the new MP-FRAP single boundary model for a barrier parallel to the optical axis, the initial underestimate is avoided and the point of onset of significant deviations greatly improves to $\sim -0.15\omega_r$.

Most MP-FRAP experiments are performed using a multiphoton laser scanning microscopy (MPLSM) platform, with a radial and axial resolution of imaging of ω_r and ω_z , respectively [26]. Based upon our results, the user can therefore image the spatial distribution of fluorophores and avoid MP-FRAP analysis using the standard model (Eq. 6) where a single barrier parallel to the optical axis is closer than $1.3 - 1.5\omega_r$. For a single barrier perpendicular to the optical axis, the onset of significant errors in the diffusion coefficient is

less than the resolution limit of MPLSM, so the conservative user would avoid MP-FRAP analysis when single barriers are closer than ω_z . To improve the range of applicability for a barrier parallel to the optical axis, the user could perform MP-FRAP analysis using the new model (Eq. 7), with which accurate diffusion coefficients can be produced down to the resolution limit, ω_r . The user is then limited in applying MP-FRAP only by the resolution limit of the lens.

B. Parallel plane boundaries

Two infinite parallel-plane reflective boundaries mimic systems such as the regions between cell walls found in tumor and brain extracellular space [23–25]. To model this system we introduce parallel-plane barriers symmetrically about the focal volume center, positioned parallel or perpendicular to the optical axis at a range of distances measured in units of ω_r or ω_z relative to the focal volume center. As before, the data is presented as D_{fit}/D_{input} as a function of boundary location. In each case, Fig. 5 shows that as the boundaries approach the focal volume, the fit diffusion coefficient begins to drop compared to the input diffusion coefficient. The fit diffusion coefficient becomes significantly different from the input diffusion coefficient as boundaries parallel to the optical axis pass $1.5\omega_r$ from the focal volume center for a high NA lens and $1.8\omega_r$ for a low NA lens. For boundaries perpendicular to the optical axis, the fit diffusion coefficient becomes statistically significantly different from the input diffusion coefficient as the boundaries pass $0.5\omega_z$ from the focal center for a high NA lens. For the low NA case, the fit diffusion does not deviate significantly for any of the boundary locations assessed.

As in the case of the single boundary, the effect on the diffusion coefficient is more significant for the case of two parallel-plane boundaries running parallel to the optical axis. As demonstrated previously, this arises because boundaries parallel to the optical axis reduce the opportunity for diffusing molecules to leave the focal volume via the shorter radial dimension, which predominantly determines the duration of recovery for a freely diffusing sample. This is also shown by the opposite behaviors of low and high NA lenses in the two geometries. When the boundaries are parallel to the optical axis, the low NA lens is the most affected because radial diffusion is more significant in this high aspect ratio focal volume. Conversely, when the boundaries are perpendicular to the optical axis, the low NA lens is

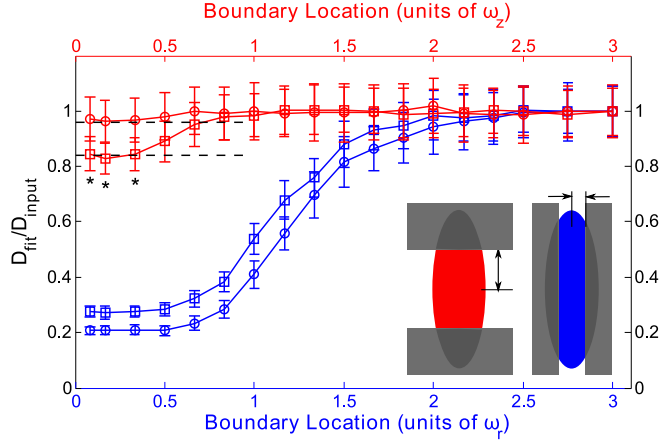


FIG. 5. Two parallel boundaries parallel (blue) or perpendicular (red) to the optical axis at a range of positions symmetric about the focal volume center and presented as fractions of ω_r or ω_z for a high NA (squares) and low NA (circles) lens. Fluorescence recovery curves were generated through Monte Carlo simulation and fit to the standard MP-FRAP model. Fit diffusion coefficients were normalized to the input diffusion coefficient, hence an accurate fit produces a ratio of one. Dashed lines mark the limit of 2D diffusion as indicated by generating data with the 2D MP-FRAP recovery equation and fitting it to the 3D MP-FRAP recovery equation. For data points marked with an asterisk (*), the accurate diffusion coefficient was recovered when the data was fit with the 2D limited MP-FRAP model.

the least affected, for the same reason. Unlike the single boundary case, however, as the boundaries significantly reduce the focal volume, the diffusion coefficient does not rise but levels off. The characteristic length of the focal volume is reduced in the direction normal to the plane surfaces, suggesting that the characteristic recovery time should become shorter, as in the single boundary case. However, as the distance between the planes approaches zero, diffusion is effectively confined to two dimensions, and this effect dominates.

By letting $\omega_z \rightarrow \infty$ in Eq. 6 we obtain a two-dimensional form of the MP-FRAP model, valid in the limit of a 2D system perpendicular to the optical axis, and which is identical to the original one-photon FRAP model [3]:

$$\frac{F(t)}{F_o} = \sum_{n=0}^{\infty} \frac{(-\beta)^n}{n!} \frac{1}{1 + n + 2nt/\tau_D}. \quad (8)$$

By generating data using this 2D formula and then fitting the data to the 3D model we find that in the limit of 2D diffusion the 3D model should yield a value of the diffusion coefficient

that is 0.84 ± 0.04 times the accepted value for a high NA lens and 0.96 ± 0.03 times the accepted value for a low NA lens. These limits are plotted in Fig. 5 as the dashed lines and coincide with the values of the normalized diffusion coefficients at small values of ω_z as determined by the Monte Carlo simulations of MP-FRAP. The asterisks(*) mark data sets that, when re-fit with the 2D MP-FRAP model given by Eq. 8, recovered the input diffusion coefficient to within one standard deviation.

To improve the accuracy of the reported diffusion coefficient for the case of parallel infinite-plane barriers to diffusion, we have derived an alternative analytical model of the fluorescence recovery (see Appendix) that takes into account the presence of the barriers. For barriers lying parallel to the optical axis, the new model is:

$$\frac{F(t)}{F_o''} = \frac{1}{3} \frac{1}{\text{erf}(2u/\omega_r)} \sum_{n=0}^{\infty} \frac{(-\beta)^n}{n!} \frac{1}{(n + \mu_n(t))} \frac{1}{(n + \nu_n(t))^{1/2}} \left\{ \text{erf} \left[-2(1 + n/\mu_n(t))^{1/2} \frac{u}{\omega_r} \right] + \exp \left[-\frac{16n}{n + \mu_n(t)} \left(\frac{u}{\omega_r} \right)^2 \right] \left(\text{erf} \left[-2 \frac{(1 - n/\mu_n(t))}{(1 + n/\mu_n(t))^{1/2}} \frac{u}{\omega_r} \right] + \text{erf} \left[-2 \frac{(1 + 3n/\mu_n(t))}{(1 + n/\mu_n(t))^{1/2}} \frac{u}{\omega_r} \right] \right) \right\}. \quad (9)$$

For barriers perpendicular to the optical axis, the form is the same but $\mu_n \rightarrow \nu_n$ and $\omega_r \rightarrow \omega_z$ in the exponential and error functions.

When the new MP-FRAP “parallel boundary” model is used to fit simulated diffusion curves produced assuming the presence of parallel-plane barriers parallel to the optical axis, the reported diffusion coefficients improve dramatically over a wide range of barrier distances (see Fig. 6). For the case of a barrier perpendicular to the optical axis the reported diffusion coefficients do not improve significantly over the already widely accurate results using the standard model (data not shown). Fig. 6 shows that the fit diffusion coefficient becomes significantly different from the input diffusion coefficient as boundaries parallel to the optical axis pass ω_r from the focal volume center for both a high and low NA lens. If the position of the boundary is not known (i.e., beyond the resolution limit of the MPLSM), we can allow u to be a free fitting parameter. However, doing so yields poor fits for sub-resolution barrier positions (data not shown).

From these simulations we have determined that when an MP-FRAP experiment is performed between parallel-plane barriers to diffusion, erroneous diffusion coefficients can be produced that underestimate D . This is caused by a hindrance of the ability of bleached molecules to leave the environment of the focal volume, coupled with an approach of the

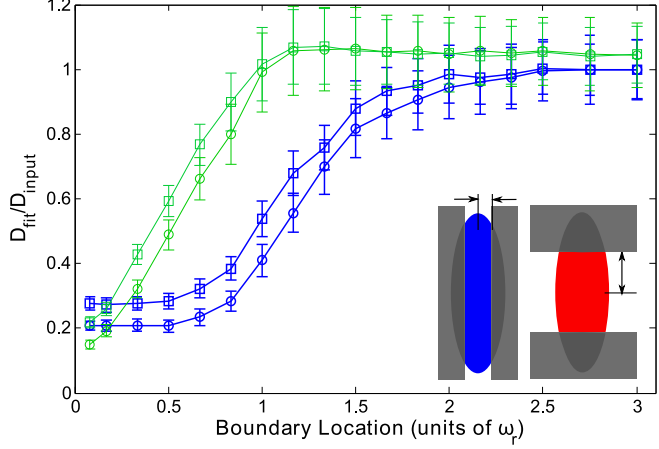


FIG. 6. Two parallel plane boundaries parallel to the optical axis at a range of positions, presented as fractions of ω_r from the focal volume center for a high NA (squares) and low NA (circles) lens. Fluorescence recovery curves were generated via Monte Carlo simulation and fit to the standard MP-FRAP model (blue) and the new MP-FRAP model (green) designed for use near a single barrier. Fit diffusion coefficients were normalized to the input diffusion coefficient, hence an accurate fit produces a ratio of one.

system to a two-dimensional geometry. The onset of these deviations is at a distance of $1.5 - 1.8\omega_r$ for barriers parallel to the optical axis, and < 0.1 to $\sim 0.5\omega_z$ for barriers perpendicular to the optical axis. Due to the high aspect ratio of two-photon focal volumes, the underestimate is most significant when the barriers are parallel to the optical axis. Based upon our results, the user can therefore image the spatial distribution of fluorophores and avoid MP-FRAP analysis using the standard model (Eq. 6) where barriers parallel to the optical axis are closer than $1.5 - 1.8\omega_r$ for high and low NA lenses, respectively. For barriers perpendicular to the optical axis, the onset of significant errors in the diffusion coefficient is less than the resolution limit of MPLSM, so the conservative user would avoid MP-FRAP analysis when single barriers are closer than ω_z . To improve the range of applicability for barriers parallel to the optical axis, the user could perform MP-FRAP analysis using the new model (Eq. 9) enabling accurate diffusion coefficients to be produced down to the resolution limit, ω_r . The user is then limited in applying MP-FRAP only by the resolution limit of the lens.

C. Cylindrical boundary

An infinite hollow cylindrical boundary provides an excellent approximation for neuronal dendrites and axons, in which transport measurements are of interest in neurobiological research [27, 28]. In our simulations we introduce a cylindrical boundary both parallel and perpendicular to the optical axis, positioned symmetrically about the focal volume center at a range of distances measured in units of ω_r and ω_z . Again, the data is presented as D_{fit}/D_{input} as a function of boundary location. As with the case of the parallel-plane boundaries, Fig. 7 shows that as the boundaries approach the focal volume, the fit diffusion coefficient begins to drop compared to the input diffusion coefficient, and these effects occur at larger values of ω_r for the case of a cylindrical boundary parallel to the optical axis than for corresponding values of ω_z in the perpendicular case. Specifically, the diffusion coefficient becomes significantly lower than the input diffusion coefficient as the radius of a cylinder parallel to the optical axis becomes smaller than $1.8\omega_r$ for a high NA lens and $2\omega_r$ for a low NA lens. The diffusion coefficient becomes statistically significantly lower than the input diffusion coefficient as the radius of a cylinder perpendicular to the optical axis becomes smaller than $0.7\omega_z$ for a high NA lens and $0.3\omega_z$ for a low NA lens.

Similar to the parallel plane boundaries, we find that when the cylindrical boundary is sufficiently constricting the diffusion effectively becomes one dimensional. Consequently, although the size of the available volume decreases there is no overestimate in the apparent D after the initial underestimate. In the limit of 1D diffusion, the MP-FRAP model can be altered to account for the dimensional change. By letting $\omega_r \rightarrow \infty$ in Eq. 6 we obtain a 1D form of the MP-FRAP model for diffusion along the optical axis:

$$\frac{F(t)}{F_o} = \sum_{n=0}^{\infty} \frac{(-\beta)^n}{n!} \frac{1}{(1 + n + 2nt/R\tau_D)^{1/2}}. \quad (10)$$

By generating data using this 1D model and fitting it to the 3D model we find that in the limit of 1D diffusion the 3D model should yield a value of the diffusion coefficient that is 0.026 ± 0.001 times the accepted value for a high NA lens and 0.006 ± 0.001 times the accepted value for a low NA lens. These limits are plotted in Fig. 7 as the dashed lines and coincide with the values of the normalized diffusion coefficients at small values of ω_r as determined by the Monte Carlo simulations of MP-FRAP. The asterisks(*) mark data sets that, when re-fit with the 1D standard MP-FRAP model, recovered the input diffusion

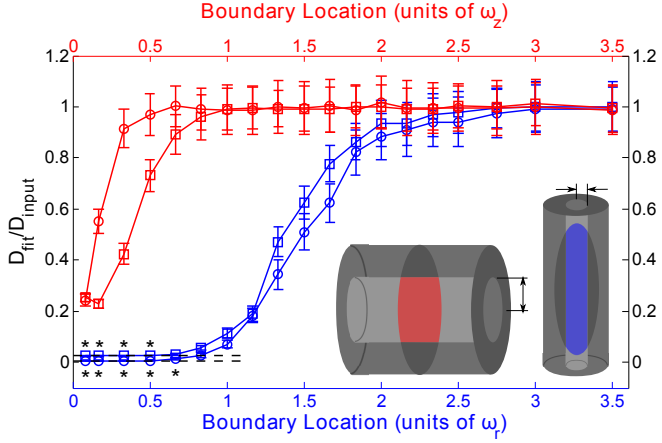


FIG. 7. Cylindrical boundary parallel (blue) and perpendicular (red) to the optical axis at a range of positions, symmetric about the focal volume center and presented as fractions of ω_r or ω_z , for a high NA (squares) and low NA (circles) lens. Fluorescence recovery curves were generated through Monte Carlo simulation and fit to the standard MP-FRAP model. Fit diffusion coefficients were normalized to the input diffusion coefficient, hence an accurate fit produces a ratio of one. Dashed lines mark the limit of 1D diffusion as indicated by generating data with the 1D MP-FRAP recovery equation and fitting it to the 3D MP-FRAP recovery equation. For data points marked with an asterisk (*), the accurate diffusion coefficient was recovered when the data was fit with the 1D limited MP-FRAP model.

coefficient, within one standard deviation.

From these simulations we have determined that when an MP-FRAP experiment is performed within an infinite cylindrical barrier to diffusion, erroneous diffusion coefficients can be produced that underestimate D . This is caused by a hindrance of the ability of bleached molecules to leave the environment of the focal volume, coupled with an approach of the system to a one-dimensional geometry. The onset of these deviations is at a radius of $\sim 1.8 - 2\omega_r$ for a cylinder parallel to the optical axis, and $\sim 0.3 - 0.7\omega_z$ for a cylinder perpendicular to the optical axis. Due to the high aspect ratio of two-photon focal volumes, the underestimate is most significant when the cylindrical barrier is parallel to the optical axis. Based upon our results, the user can therefore image the spatial distribution of fluorophores and avoid MP-FRAP where the cylinder parallel to the optical axis has a radius smaller than $\sim 1.8\omega_r$. A cylinder perpendicular to the optical axis rests in the image plane, and can be

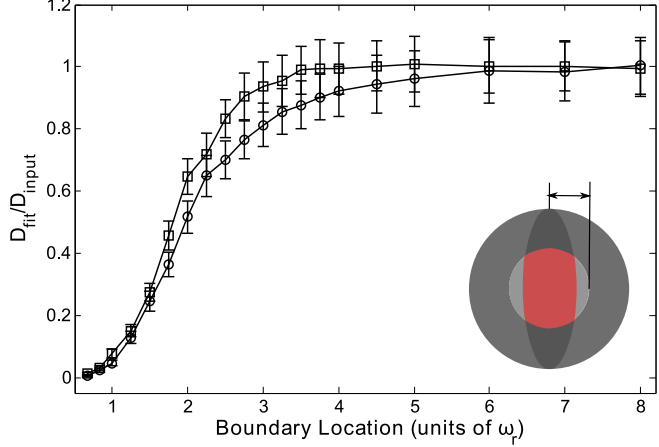


FIG. 8. Spherical boundary at a range of positions, symmetric about the focal volume center and presented as fractions of ω_r , for a high NA (squares) and low NA (circles) lens. Fluorescence recovery curves were generated through Monte Carlo simulation and fit to the standard MP-FRAP model. Fit diffusion coefficients were normalized to the input diffusion coefficient, hence an accurate fit produces a ratio of one.

imaged with the superior ω_r radial resolution of imaging. Hence the radius of the cylinder can be readily determined down to a resolution significantly smaller than ω_z and the user would avoid cylinders that have a radius smaller than $\sim 0.7\omega_z$.

D. Spherical boundary

A hollow spherical boundary well approximates a cell body, cell nucleus or dendritic spine [29–31]. We introduce the spherical boundary symmetrically about the focal volume center at a range of distances measured in units of ω_r . The data is presented as D_{fit}/D_{input} as a function of boundary location. Fig. 8 shows that the fit diffusion coefficient drops rapidly relative to the input diffusion coefficient as the boundaries narrow in on the focal volume. Specifically, the diffusion coefficient becomes significantly lower than the input diffusion coefficient as the radius of the sphere becomes smaller than $2.75\omega_r$ for a high NA lens and $3.75\omega_r$ for a low NA lens.

As the sphere becomes sufficiently small, many (and eventually all) of the bleached molecules will be unable to leave the focal volume. This suggests that the standard 3D MP-FRAP model (Eq. 6), which assumes free diffusion of the entire fluorophore population,

may be inappropriate to fit the recovery. The concept of an “immobile fraction” has been discussed previously [1, 32] in the context of fluorophore populations attached to the extracellular matrix or cell cytoskeleton, and involves an additional fitting parameter to account for the incomplete recovery caused by a subset of immobile fluorophores. We refit the data generated for free diffusion within a spherical boundary using standard 3D MP-FRAP with a fitting parameter for an immobile fraction, but did not achieve significantly more accurate values for the diffusion coefficient (data not shown). This arises because the case of an immobile fluorophore population and our case of a trapped but mobile population are only superficially similar. In the case of an immobile fraction, a subset of fluorophores are permanently (relative to the duration of the experiment) fixed in space. The remaining fluorophores, however, are assumed to diffuse freely. In the case of fluorophores confined within a spherical boundary, however, while many fluorophores remain within the focal volume they are always free to move. As the bleached molecules spread from their initial center-heavy distribution to a more uniform distribution, the fluorescence of the sample changes. The shape of the recovery is subtly, yet significantly different from the case of immobile fluorophores, and fitting with this added parameter does not significantly improve the resultant diffusion coefficient.

From these simulations we have determined that when an MP-FRAP experiment is performed within a spherical barrier to diffusion, erroneous diffusion coefficients can be produced which underestimate D . This is caused by a hindrance of the ability of bleached molecules to leave the environment of the focal volume. The onset of these deviations is at a radius of $\sim 2.75 - 3.75\omega_r$ and is not improved by fitting with an immobile fraction term. This radius is significantly greater than the ω_r resolution of imaging of MPLSM systems. Therefore, based upon our results, the user can image the spatial distribution of fluorophores and avoid MP-FRAP within spherical compartments where the sphere has a radius smaller than $\sim 3.75\omega_r$.

IV. CONCLUSION

In this paper, we have used Monte Carlo simulations to model multiphoton fluorescence recovery after photobleaching in the presence of reflecting boundaries of various geometries and sizes. Our results show that MP-FRAP can produce erroneous values of the diffusion

coefficient even when the boundaries are significantly larger than the focal volume. The size limit at which the boundaries begin affecting the MP-FRAP measurement varies with the geometry of the boundary, with the two extremes being a single plane perpendicular to the optical axis (D becomes erroneous at $\sim -0.3\omega_z$) and a sphere (D becomes erroneous at $3.75\omega_r$). The significance of the error is a function of the aspect ratio of the focal volume (i.e., the NA) and the orientation of the barriers, with barriers to diffusion in the radial direction having the greatest effect. Using our guidelines, a researcher can first image a sample using two-photon fluorescence, then measure and locate a region with the appropriate dimensions to allow an accurate measurement of the diffusion coefficient using the appropriate model. For both a single and paired barriers parallel to the optical axis, we present a new model of MP-FRAP that can be used to produce accurate diffusion coefficients for boundary distances much closer than is possible with the standard MP-FRAP model. Measurements of diffusion via MP-FRAP can now be completed with confidence in an array of *in vivo* systems previously believed to be inaccessible.

Appendix

The time-dependent concentration distribution of unbleached fluorophore following the bleach pulse is given by Brown et. al. [1]. When written in Cartesian coordinates for a concentration distribution centered at the origin, the expression is:

$$c(x, y, z; t) = c_o \sum_{n=0}^{\infty} \frac{(-\beta)^n}{n!} \frac{1}{\mu_n(t) \nu_n(t)^{1/2}} \exp \left[-\frac{2bn}{\omega_r^2} \frac{x^2}{\mu_n(t)} \right] \exp \left[-\frac{2bn}{\omega_r^2} \frac{y^2}{\mu_n(t)} \right] \exp \left[-\frac{2bn}{\omega_z^2} \frac{z^2}{\nu_n(t)} \right], \quad (\text{A.1})$$

where

$$\mu_n(t) = 1 + 8bnDt/\omega_r^2, \quad (\text{A.2})$$

$$\nu_n(t) = 1 + 8bnDt/\omega_z^2. \quad (\text{A.3})$$

For the case of a single infinite plane boundary at the origin we can develop an approximate analytical model by replacing the barrier with the real distribution and an “image” distribution placed symmetrically about the origin at a positions u and $-u$, which represent the distance of the real distribution from the barrier (see Fig. 9). In the region to the right of the origin, this closely models the behavior of the system: as the distributions spread due to

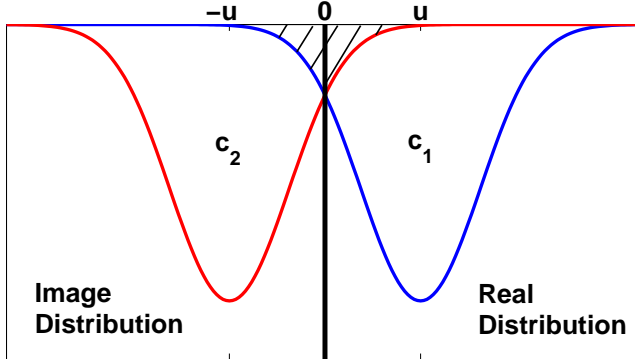


FIG. 9. Placement of real and “image” bleached molecule concentration distributions for the case of a single infinite plane boundary. The overlap of the image distribution in the region of the real distribution as the two distributions spread ($t > 0$) mimics the behavior of diffusing molecules that bounce off the barrier and back into the focal volume. At $t = 0$, there will be overcounting of bleached molecules when the two distributions are close to the barrier. This error will remain small until the image distribution peak approaches the barrier.

diffusion, the overlap of the image distribution with the real distribution mimics the behavior of those fluorophores that bounce off the barrier and back into the space to the right of the barrier. With this approximation, there is some over counting of the initial fluorophore population (hatched region in Fig. 9) when the two distributions are oriented close to the barrier. This “extra” distribution of bleached molecules will evolve over time, producing an error in the fluorescence as a function of time, and hence in the diffusion coefficient, D . However, this error remains small until the peak of the image distribution approaches the origin. As the two distributions perfectly overlap the error in D disappears, then grows again as the distribution centers continue past one another. The combined concentration distribution, assuming a barrier parallel to the optical axis in the x-dimension, is given by

$$c'(x, y, z; t) = (1/2)[c_1(x - u, y, z; t) + c_2(x + u, y, z; t)], \quad (\text{A.4})$$

where c_1 and c_2 are produced by introducing a coordinate shift into Eq. A.1, and the $1/2$ accounts for the fact that we have introduced an image distribution that doubles the true concentration of fluorophore.

The fluorescence recovery is monitored by a low-intensity laser beam centered on the real

concentration distribution, and is given by

$$F'(t) = \frac{\delta_m E}{2m} \int \langle I_{mo}^m(x - u, y, z) \rangle c'(x, y, z; t) dx dy dz, \quad (\text{A.5})$$

where δ_m is the multiphoton fluorescence action cross section, E is the collection efficiency of the system, m is the number of photons required to produce fluorescence from a single fluorophore, and $\langle I_{mo}^m(x - u, y, z) \rangle$ is the time-average of the bleach intensity raised to the m^{th} power, given by

$$\langle I_{mo}^m(x - u, y, z) \rangle = \langle I_{mo}^m(0, 0, 0) \rangle e^{-(2m/\omega_r^2)(x-u)^2} e^{-(2m/\omega_r^2)y^2} e^{-(2m/\omega_z^2)z^2}. \quad (\text{A.6})$$

It is important to note that while for the standard model derivation the integral in $F(t)$ is taken over all space, in the presence of a single barrier the integral along the dimension interrupted by the barrier (in this case x) is taken only from $0 \rightarrow \infty$.

When Eqs. A.4 and A.6 are substituted into Eq. A.5 and the integral is performed, the simplified expression for the fluorescence recovery, letting $m = b = 2$ is:

$$\begin{aligned} \frac{F'(t)}{F'_o} &= \frac{1}{2} \frac{1}{\text{erfc}(-2u/\omega_r)} \sum_{n=0}^{\infty} \frac{(-\beta)^n}{n!} \frac{1}{(n + \mu_n(t))} \frac{1}{(n + \nu_n(t))^{1/2}} \\ &\times \left\{ \text{erfc} \left[-2(1 + n/\mu_n(t))^{1/2} \frac{u}{\omega_r} \right] + \exp \left[-\frac{16n}{n + \mu_n(t)} \left(\frac{u}{\omega_r} \right)^2 \right] \text{erfc} \left[-2 \frac{(1 - n/\mu_n(t))}{(1 + n/\mu_n(t))^{1/2}} \frac{u}{\omega_r} \right] \right\}, \end{aligned} \quad (\text{A.7})$$

where F'_o is the equilibrium value of the fluorescence before the photobleaching pulse. We can compare Eq. A.7 with the standard MP-FRAP model (Eq. 6) to gain some insight into the new form. As noted earlier, the $1/2$ arises from our introduction of the image distribution. The first complementary error function comes from the calculation of F'_o , which is evaluated over the limits $0 \rightarrow \infty$. The first part of the summation, appearing on the first line, is the standard MP-FRAP equation. Finally, the contribution to the fluorescence recovery is shared between the real concentration distribution, represented by the second complementary error function, and the image concentration distribution, represented by the exponential \times complementary error function term. In the limit $u \rightarrow \infty$,

$$\frac{F'(t)}{F'_o} = \frac{1}{2} + \frac{1}{2} \sum_{n=0}^{\infty} \frac{(-\beta)^n}{n!} \frac{1}{(n + \mu_n(t))} \frac{1}{(n + \nu_n(t))^{1/2}}. \quad (\text{A.8})$$

With the image distribution center pushed to negative infinity, the distribution of unbleached molecules in the region of the focal volume (at positive infinity) is at equilibrium, and

contributes a constant $1/2$ to the normalized fluorescence. Meanwhile, the real distribution center translates to infinity with the focal volume, and produces a fluorescence recovery with the same form as a standard fluorescence recovery. At full recovery ($t \rightarrow \infty$), $F'(t)/F'_o = 1$, as expected.

This derivation can be repeated for a wall perpendicular to the optical axis by introducing the appropriate coordinate shifts in z , rather than x or y . The result has the same form as Eq. A.7, but with $\omega_r \rightarrow \omega_z$ and $\mu_n(t) \rightarrow \nu_n(t)$ in the exponential and complimentary error functions.

Following similar logic leading to the derivation of the “one boundary” MP-FRAP model, we can also produce an approximate analytical model for use in the presence of two parallel infinite-plane boundaries. In this case, we place the real concentration distribution at the origin, and model two boundaries placed symmetrically about the distribution center (at u and $-u$) with an image distribution on the opposite side of each barrier (at $-2u$ and $2u$). The concentration distribution for this configuration has three parts, $c''(x, y, z; t) = (1/3)[c_1(x - 2u, y, z; t) + c_2(x, y, z; t) + c_3(x + 2u, y, z; t)]$, and the integration to determine the fluorescence is limited to $-u \rightarrow u$ along the dimension in which the barriers appear. The resulting normalized fluorescence recovery, for boundaries parallel to the optical axis, is given by:

$$\begin{aligned} \frac{F''(t)}{F''_o} = & \frac{1}{3} \frac{1}{\text{erf}(2u/\omega_r)} \sum_{n=0}^{\infty} \frac{(-\beta)^n}{n!} \frac{1}{(n + \mu_n(t))} \frac{1}{(n + \nu_n(t))^{1/2}} \left\{ \text{erf} \left[-2(1 + n/\mu_n(t))^{1/2} \frac{u}{\omega_r} \right] \right. \\ & \left. + \exp \left[-\frac{16n}{n + \mu_n(t)} \left(\frac{u}{\omega_r} \right)^2 \right] \left(\text{erf} \left[-2 \frac{(1 - n/\mu_n(t))}{(1 + n/\mu_n(t))^{1/2}} \frac{u}{\omega_r} \right] + \text{erf} \left[-2 \frac{(1 + 3n/\mu_n(t))}{(1 + n/\mu_n(t))^{1/2}} \frac{u}{\omega_r} \right] \right) \right\}. \end{aligned} \quad (\text{A.9})$$

Similar to the single boundary formula, the $1/3$ arises from the introduction of the two image distributions. The first error function comes from the calculation of F''_o , which is evaluated from $-u \rightarrow u$. The standard MP-FRAP model appears again, and is weighted by contributions from the real distribution, represented by the second error function, and the image distributions, represented by the two exponential \times error function terms. In the limit $u \rightarrow \infty$,

$$\frac{F''(t)}{F''_o} = \frac{2}{3} + \frac{1}{3} \sum_{n=0}^{\infty} \frac{(-\beta)^n}{n!} \frac{1}{(n + \mu_n(t))} \frac{1}{(n + \nu_n(t))^{1/2}}. \quad (\text{A.10})$$

Here, the image distributions contribute a constant $1/3$ each to the normalized fluores-

cence, while the real distribution recovers as would a standard MP-FRAP curve. At full recovery ($t \rightarrow \infty$), $F(t)''/F_o'' = 1$, as expected.

As with the one boundary model, this derivation can be repeated for walls perpendicular to the optical axis by introducing the appropriate coordinate shifts in z , rather than x or y . The result has the same form as Eq. A.9, but with $\omega_r \rightarrow \omega_z$ and $\mu_n(t) \rightarrow \nu_n(t)$ in the exponential and error functions.

ACKNOWLEDGMENTS

The authors would like to thank Matthew C. Sullivan for several useful conversations. This work was supported by a Department of Defense Era of Hope Scholar Award (No. W81XWH-05-1-0396), an NIH Directors New Innovator Award (No. 1DP2OD006501-01), and by the Pew Scholars Program in the Biomedical Sciences (Edward Brown).

- [1] E. B. Brown, E. S. Wu, W. Zipfel, and W. W. Webb, *Biophys. J.*, **77**, 2837 (1999).
- [2] W. Denk, J. H. Strickler, and W. W. Webb, *Science*, **248**, 73 (1990).
- [3] D. Axelrod, D. E. Koppel, J. Schlessinger, E. Elson, and W. W. Webb, *Biophys. J.*, **16**, 1055 (1976).
- [4] M. Edidin, M. Zagyansky, and T. Lardner, *Science*, **191**, 466 (1976).
- [5] D. E. Koppel, D. Axelrod, J. Schlessinger, E. L. Elson, and W. W. Webb, *Biophys. J.*, **16**, 1315 (1976).
- [6] D. A. Berk, F. Yuan, M. Leunig, and R. K. Jain, *Biophys. J.*, **65**, 2428 (1993).
- [7] D. Magde, E. L. Elson, and W. W. Webb, *Biopolymers*, **13**, 29 (1974).
- [8] H. Qian, M. P. Sheetz, and E. L. Elson, *Biophys. J.*, **60**, 910 (1991).
- [9] K. M. Berland, P. T. C. So, and E. Gratton, *Biophys. J.*, **68**, 694 (1995).
- [10] J. Mertz, C. Xu, and W. W. Webb, *Opt. Lett.*, **20**, 2532 (1995).
- [11] W. Watanabe, S. Matsunaga, T. Higashi, K. Fukui, and K. Itoh, *J. Biomed. Opt.*, **13**, 031213 (2008).
- [12] R. M. Williams, W. R. Zipfel, M. L. Tinsley, and C. E. Farnum, *Biophys. J.*, **93**, 1039 (2007).
- [13] S. Basu, V. Rodionov, M. Terasaki, and P. J. Campagnola, *Opt. Lett.*, **30**, 159 (2005).

[14] K. D. Sullivan, W. H. Sipprell III, E. B. Brown Jr., and E. B. Brown III, *Biophys. J.*, **96**, 5082 (2009).

[15] S. Coscoy, F. Waharte, A. Gautreau, M. Martin, D. Louvard, P. Mangeat, M. Arpin, and F. Amblard, *Proc. Natl. Acad. Sci. USA*, **99**, 12813 (2002).

[16] F. Waharte, C. M. Brown, S. Coscoy, E. Coudrier, and F. Amblard, *Biophys. J.*, **88**, 1467 (2005).

[17] D. M. Soumpasis, *Biophys. J.*, **41**, 95 (1983).

[18] F. P. Coelho, W. L. Vaz, and E. Melo, *Biophys. J.*, **72**, 1501 (1997).

[19] M. J. Saxton, *Biophys. J.*, **81**, 2226 (2001).

[20] E. Brown and W. Webb, “Caged compounds. methods of enzymology series v. 291,” (Academic Press, 1998) Chap. Two-Photon Activation of Caged Calcium with Submicron, Submillisecond Resolution, pp. 356–380.

[21] P. K. Tsourkas, M. L. Longo, and S. Raychaudhuri, *Biophys. J.*, **95**, 1118 (2008).

[22] S. Wieser, M. Axmann, and G. J. Schütz, *Biophys. J.*, **95**, 5988 (2008).

[23] G. Alexandrakis, E. B. Brown, R. T. Tong, T. D. McKee, R. B. Campbell, Y. Boucher, and R. K. Jain, *Nat. Med.*, **10**, 203 (2004).

[24] D. K. Binder, M. C. Papadopoulos, P. M. Haggie, and A. S. Verkman, *J. Neurosci.*, **24**, 8049 (2004).

[25] M. C. Papadopoulos, J. K. Kim, and A. S. Verkman, *Biophys. J.*, **89**, 3660 (2005).

[26] W. R. Zipfel, R. M. Williams, and W. W. Webb, *Nat. Biotechnol.*, **21**, 1369 (2003).

[27] M. Gabso, E. Neher, and M. E. Spira, *Neuron*, **18**, 473 (1997).

[28] H. Schmidt, O. Arendt, E. B. Brown, B. Schwaller, and J. Eilers, *J. Neurochem.*, **100**, 727 (2007).

[29] K. Svoboda, D. W. Tank, and W. Denk, *Science*, **272**, 716 (1996).

[30] A. Majewska, E. Brown, J. Ross, and R. Yuste, *J. Neurosci.*, **20**, 1722 (2000).

[31] K. Holthoff, D. Tsay, and R. Yuste, *Neuron*, **33**, 425 (2002).

[32] T. J. Feder, I. Brust-Mascher, J. P. Slattery, B. Baird, and W. W. Webb, *Biophys. J.*, **70**, 2767 (1996).

Thermally activated diffusion in reversibly associating polymers†

Jiahui Li,^a Kelley D. Sullivan,^b Edward B. Brown^c and Mitchell Anthamatten^{*a}

Received 19th May 2009, Accepted 13th October 2009

First published as an Advance Article on the web 21st October 2009

DOI: 10.1039/b909662k

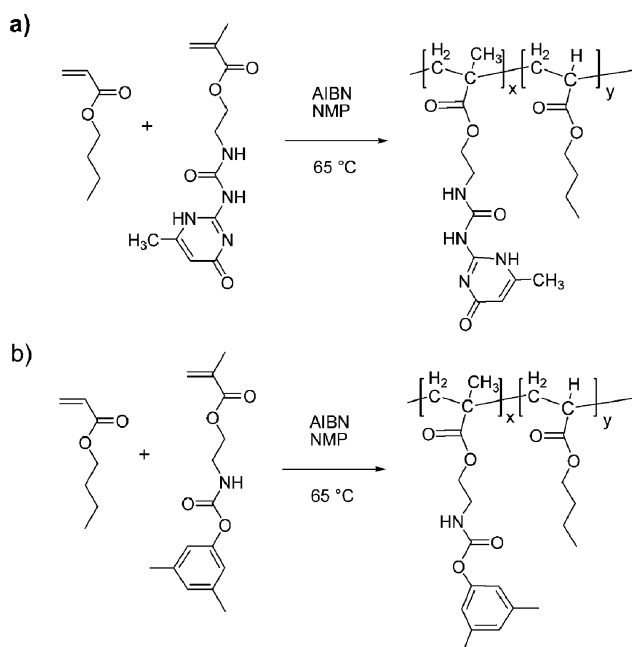
Mass transport of a small molecule dye through dynamic polymer networks containing reversibly associating side-groups was directly compared to steady-shear viscosity measurements suggesting that viscous relaxation is limited more by the frequency of dissociation events while mass transport is determined primarily by the degree of association.

The mission to understand structure–property relationships of polymers bearing reversibly associating functional groups has opened a new field at the interface of polymers and supramolecular chemistry. Reversible binding through cooperative hydrogen bonds, ionic interactions, and metal–ligand complexes can lead to aggregation, gelation, or sudden viscosity changes that are triggered by changes in polymer concentration, pH, or temperature.^{1,2} In the melt, rigid and elastic dynamic networks can be transformed into low viscosity melts, simply by heating. This material concept has engendered new shape memory polymers, thermoplastic elastomers, and self-healing materials.^{3–6} These and other studies have highlighted the role that reversible interactions play in influencing the dynamics of viscous relaxation.

Understanding the dissociation kinetics of supramolecular polymers is paramount in developing responsive materials. Dissociation of dimers or aggregates is thermally activated and can be directly related to mechanical properties.^{3,7–9} At low temperatures, the rate of dissociation is sluggish and limits viscous relaxation of chains. At higher temperatures reversible interactions exhibit rapid exchange resulting in lower modulus and rapid stress relaxation.

To our knowledge, no singular study has been performed to examine how mass transport of small molecules through polymer melts is influenced by reversible interactions. Understanding and controlling mass transport through amorphous polymers is an important aspect of emerging technologies including drug delivery, chemical sensors, and barrier elastomers. We are studying copolymers containing reversibly associating side-groups. In this Communication, we report a side-by-side comparison of how side-group association affects mechanical properties and mass transport in polymer melts. Our findings indicate that mass transport is not determined by the kinetics of side-group dissociation, but more by the overall equilibrium constant between free and associated side-groups.

A remarkably versatile H-bonding motif is the ureidopyrimidinone (UPy) functional group.² The UPy group contains four in-plane hydrogen bonds that act cooperatively to yield unusually high solution self-dimerization constants ($\sim 10^7$ mol⁻¹ in CHCl₃).¹⁰ In addition to its high binding energy (~ 70 kJ mol⁻¹), the UPy group is an attractive synthon because it is straightforward to synthesize. Reversibly associating copolymers (RACs) containing butyl acrylate and UPy-functionalized ethyl methacrylate monomers were prepared using conventional free radical polymerization (see Scheme 1). Control copolymers (CCPs) containing 3,5-dimethylphenyl urethane (DMPU) side-groups were also prepared as a control group. The DMPU side-group is about the same size and shape as the UPy group, but it is not expected to undergo significant self-dimerization. Polymerizations were conducted at 65 °C for eight hours in N-methylpyrrolidone (NMP) using azobisisobutyronitrile (AIBN) as an initiator.⁴ The products were precipitated twice into a water–methanol (1 : 10) solution to ensure the product was free of unreacted monomer. Functional polymers were characterized using ¹H NMR and gel permeation chromatography (Viscotek, Agilent 1100), and results are summarized in Table 1. The composition of polymer samples withdrawn after half an hour of reaction time (from ¹H NMR) showed close agreement with final product composition indicating that the polymer products are nearly random copolymers



Scheme 1 Synthesis of poly(butyl acrylate) copolymers containing (a) H-bonding (UPy) side-groups and (b) non-H-bonding DMPU side-groups.

^aDepartment of Chemical Engineering, University of Rochester, Rochester, NY 14627, USA. E-mail: anthamatten@che.rochester.edu

^bDepartment of Physics and Astronomy, University of Rochester, Rochester, NY 14627, USA

^cDepartment of Biomedical Engineering, University of Rochester, Rochester, NY 14627, USA

† Electronic supplementary information (ESI) available: ¹H NMR analysis, GPC and viscosity measurements. See DOI: 10.1039/b909662k

Table 1 Molecular weight characteristics of synthesized reversibly associating copolymers (RACs) and control copolymers (CCPs)

Name	Side-group content		M_n ^b	PDI ^b
	Substituent feed/mol%	Measured $\alpha/\text{mol}\%$		
PBA	0	0	14 100	1.53
RAC-1	1.0	0.84	16 500	2.00
RAC-2	2.0	1.68	12 600	2.11
CCP-1	1.0	1.10	13 509	2.36
CCP-2	2.0	1.95	14 920	2.45

^a ^1H NMR. ^b GPC.

and do not have significant composition gradients. Polymers were synthesized to molecular weights between 12–16 kg mol⁻¹—below the entanglement molecular weight.¹¹

Diffusion through synthesized polymers was studied using multi-photon fluorescence recovery after photobleaching (MP-FRAP, see Fig. 1). MP-FRAP measures 3-D mobility of fluorescent molecules with well defined bleaching geometry and a spatial resolution of less than a micron. FRAP is often used to study diffusion in biological systems, but has recently proven useful to study diffusion through polymer melts.^{12–14} Unlike conventional (one photon) FRAP, the

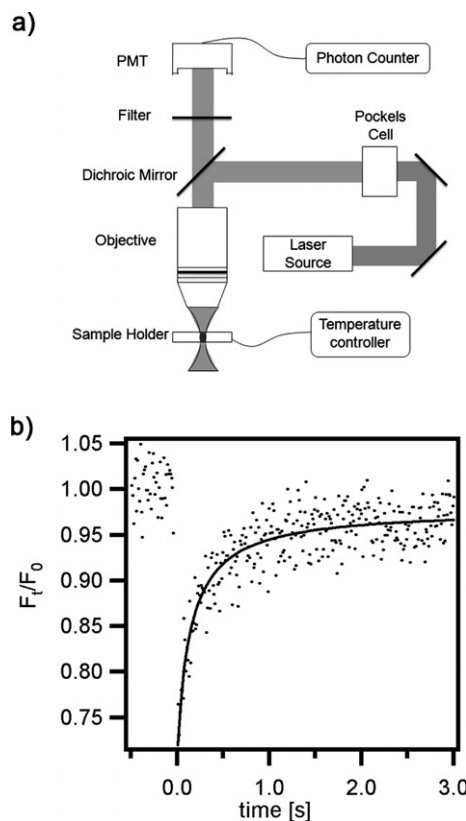


Fig. 1 MP-FRAP of reversibly associating polymers: (a) experimental setup, and (b) example of fluorescence recovery curve (RAC-1) with 20 M rhodamine 6G at 60 °C. This sample was photobleached using 810 nm light (350 mW) for 10 ms, and subsequent fluorescence was monitored at a reduced power of 35 mW. The dark line is a non-linear regression, least squares fit, to eqn (1) by varying β , F_0 and τ_D .

three-dimensional resolution of MP-FRAP renders it insensitive to sample thickness, facilitating measurement of bulk diffusion coefficient of dyes through the copolymers.

Diffusion of rhodamine 6G dye through synthesized polymers was studied between 20 and 80 °C. The fraction of recovered fluorescence, F_t/F_0 , was recorded against time t and fit using:

$$F_t/F_0 = \sum_{n=0}^{\infty} \frac{(-\beta)^n}{n!} \frac{1}{1+n+2nt/\tau_D} \frac{1}{\sqrt{1+n+2nt/R\tau_D}} \quad (1)$$

where β is the bleach depth; R and τ_D are defined by

$$R \equiv w_z^2/w_r^2 \quad (2)$$

and

$$\tau_D \equiv w_r^2/8D \quad (3)$$

where w_r and w_z are focal area radial and axial dimensions and D is the dye diffusion coefficient.¹⁵ Raw recovery data were fitted using three parameters: β , F_0 and τ_D . The diffusion coefficient D was then obtained using eqn (3). Attempts were made fitting only two parameters (β and τ_D), however the quality of fit was significantly lower. The two-parameter fitted curve typically overshoots the data at early time and results in a higher values of D . Nevertheless, both methods revealed similar trends leading to the same conclusion. To reduce uncertainty D , only values from three-parameter fits are reported.

An Arrhenius plot of measured dye diffusion coefficients through synthesized copolymers is shown in Fig. 2. Clearly, the presence of UPy associating side-groups, inhibits dye diffusion. The dye diffusivity is reduced by nearly an order of magnitude in the sample containing 1.7 mol% of UPy side-groups. However, the concentration of UPy side-groups has little effect on the diffusion activation energy, E_a , and all reversibly associating copolymers have about the same activation energies (~ 50 kJ mol⁻¹). These trend are similar to those observed in polymers containing permanent crosslinks.¹⁶

To verify that the observed reduction of penetrant diffusion is due to side-group association, instead of an anti-plasticizer effect, control copolymers containing DMPU side-groups were examined (Fig. 2b). Compared to the poly(butyl acrylate) sample, the DMPU side-groups also exhibited lower dye diffusivity. However, this effect was much smaller than that observed in UPy-containing samples, suggesting that associating side-groups at least partly explains the reduction in dye diffusivity. Diffusion through the DMPU-containing samples may also be influenced by aggregation of DMPU side-groups, and, more importantly, by molecular weight effects. The molecular weight appears to influence dye diffusivity in all samples, explaining more subtle differences between data sets. For example, RAC-1 has a significantly higher molecular weight (16.5 k) than RAC-2 (12.6 k). This explains why dye diffusion through RAC-1, with only 0.8 mol % of UPy-groups, is reduced nearly to the level of RAC-2. Furthermore, CCP-2 has a rather high molecular weight (14.9 k) which may partly explain the decrease in dye diffusivity. Note that CCP-1 and the control sample PBA have almost the same molecular weight, and their diffusion data are nearly superimposed in Fig. 2b.

As a further comparison, we prepared a crosslinked poly(butyl acrylate) containing 1 mol% ethylene glycol diacrylate (EGDA). The sample was loaded with dye and studied using MP-FRAP over the

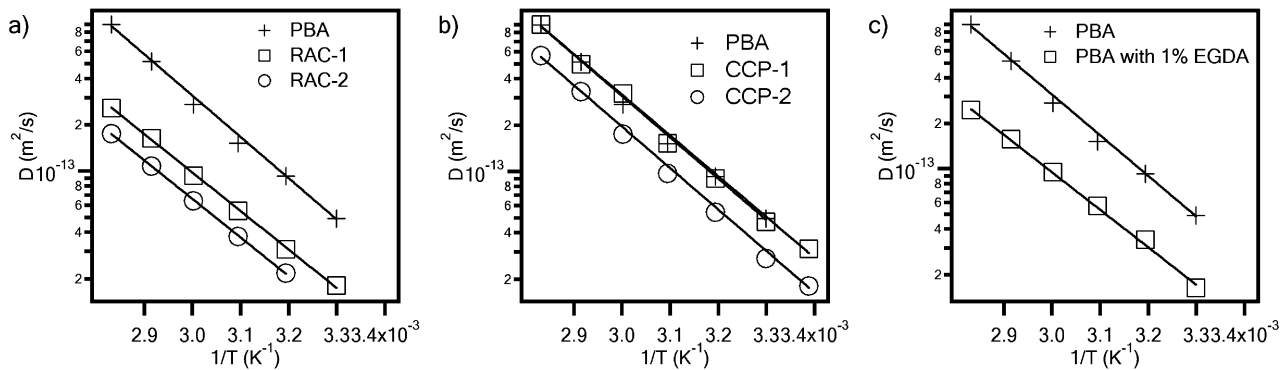


Fig. 2 Arrhenius plot of dye diffusion coefficient through different polymers: (a) poly(butyl acrylate) ($E_a = 51.4 \pm 4.4 \text{ kJ mol}^{-1}$) and associating copolymers containing 0.8 and 1.7 mol% UPy side-groups ($E_a = 47.8 \pm 2.1, 47.9 \pm 1.3 \text{ kJ mol}^{-1}$), (b) poly(butyl acrylate) and control copolymers containing 1.1 mol% and 2.0 mol% DMPU side-groups ($E_a = 50.7 \pm 3.6, 51.6 \pm 2.9 \text{ kJ mol}^{-1}$), and (c) poly(butyl acrylate) and crosslinked poly(butyl acrylate) with 1 mol % of EGDA as crosslinker ($E_a = 47.4 \pm 2.8 \text{ kJ mol}^{-1}$). Reported errors in E_a reflect 95% confidence intervals and were obtained from least-squares fitting.

same temperature range. Resulting diffusion coefficients are shown in Fig. 2c. Comparing to Fig. 2a, it appears that non-covalent crosslinks hinder dye diffusion in a similar manner as permanent crosslinks. Both types of crosslinks lower the diffusion coefficient however do not significantly change the diffusion activation energy.

Where MP-FRAP uniquely enables molecular diffusion to be studied, it is well known that the rate of viscous relaxation of reversibly associating copolymers is thermally activated. At low temperatures, polymers containing associating groups exhibit higher storage modulus and melt viscosities compared to polymers without associating groups.²⁻⁴ Steady-shear experiments were conducted on synthesized polymers to enable a direct comparison of diffusion and stress relaxation dynamics. Viscosity data obtained at different temperatures are plotted in Fig. 3. Samples with higher UPy content showed both higher viscosities and higher activation energies. In contrast, the DMPU side-groups in the control copolymer had little effect on measured viscosity. These features are consistent with our prior study of shape-memory polymers which showed viscous relaxation is limited by the rate of side-group dissociation.³ Activation energies of linear PBA are in rough agreement with steady-shear data obtained by Yanamaguchi *et al.*⁴ Note, from Rubinstein's theory of thermoreversible gels, that the activation energies from Fig. 3 may be appreciably higher than those from dissociation of two isolated stickers since the lifetime of a free UPy group may be small relative to the timescale of network rearrangement.¹⁷ In other words, multiple dissociation and recombination events may occur between the same dimer pair before the network topology changes. Remarkably, the heightened activation energy observed in steady-shear experiments is not apparent in the MP-FRAP data (Fig. 2), suggesting a fundamental difference between diffusive transport through RACs and their viscous relaxation.

Together, steady-shear and MP-FRAP experiments suggest that, for the dynamic copolymers studied here, viscous relaxation is influenced more by the H-bonding dissociation rate (k_d), while small molecule diffusion is influenced more by the H-bonding equilibrium value (K). In the case of steady-shear, when an H-bond dissociates, the material can more readily deform under a lower stress field as indicated schematically in Fig. 3b. Consequently, shear rate and viscosity are inherently tied to the rate of H-bonding dissociation. This explains the observation of higher viscosities and higher

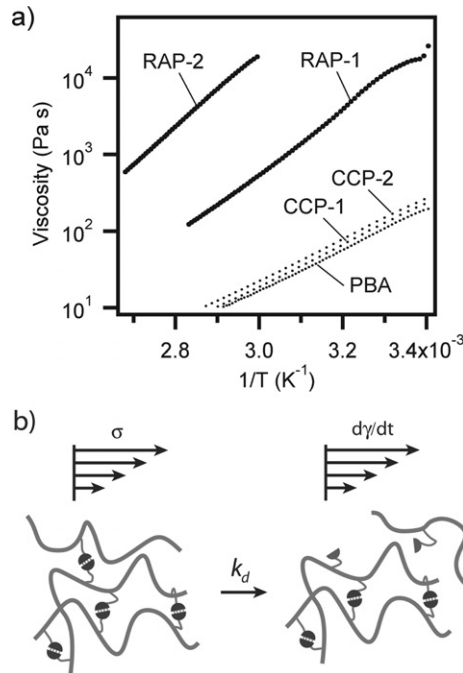


Fig. 3 (a) Viscosities of polymers containing UPy H-bonding groups measured at a radial shear rate of 0.1 rad/s. (b) Schematic illustrating viscous relaxation under shear stress (σ) in a dynamic polymer network containing self-complementary, reversible H-bonding groups.

activation energies for UPy containing polymers. Following dissociation, a free associating group can only associate with a similarly free species. Under steady-shear, a dissociated dimer is less likely to reassociate with its original partner because of the imposed strain field. Along these lines, one expects that the extent of dimerization under steady-shear may be lower than that in a static state, however, this has not yet been confirmed experimentally.

On the other hand, small molecule diffusion through UPy containing copolymers is not under the influence of mechanical stress, and associating groups can repeatedly dissociate and rebond with the same species. In this scenario, the relevant kinetics (of the diffusion process) are limited by the overall concentration H-bonding

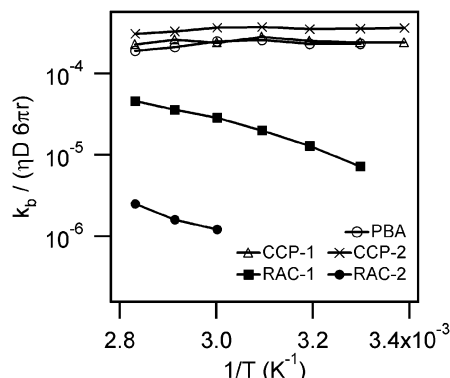


Fig. 4 Plot of $k_b / (\eta D 6\pi r)$ versus $1/T$ for poly(butyl acrylate), synthesized control copolymers (CCPs), and reversibly associating copolymers.

side-groups. The number of H-bonding crosslinks are determined by the equilibrium constant K which defines the degree of H-bonding association. Although the van't Hoff relationship predicts that this equilibrium is also temperature dependent, the literature suggests that UPy H-bonding equilibrium is strongly in favor of the association state, even at 120 °C.¹⁸ Therefore, while the presence of UPy H-bonding groups lowers the absolute value of diffusion coefficient, it does not change the activation energy in the same manner as it does for viscous relaxation. At higher temperatures, when K is of the order of unity, this situation may be different, and the copolymer curves in Fig. 2 are expected to fall upon the unfunctionalized PBA curve. This may be the subject of a future study.

The diffusion results in Fig. 2 can be also be contrasted with dynamic light scattering studies of colloid particles diffusing through solutions of reversibly associating polymers.^{19,20} In the limit of long time-scales, Brownian diffusion dynamics are determined by the macroscopic viscosity of the surrounding polymer solution. However, if the probe size is much smaller than the correlation length of the polymer network, then the diffusion is faster than expected. The present study examines the diffusion of a small molecule dye, with a nanometer length scale. Considering the viscous properties of the surrounding networks, our data also show that diffusion is significantly faster than expected at all temperatures. Fig. 4 shows a plot of the product $k_b / (\eta D 6\pi r)$ (from the Stokes-Einstein equation) versus inverse temperature where k_b is Boltzman's constant, η is melt viscosity, and r is the radius of the diffusing dye, estimated to be 5 Å. This product is constant for PBA and for the control copolymers (CCPs) but it decreases with $1/T$ for the reversibly associating polymers. This decrease indicates that changes in viscosity are incommensurate with changes in dye diffusivity.

In conclusion, multi-photon fluorescence recovery after photobleaching was demonstrated as an effective tool for studying dye diffusion through reversibly associating polymer melts. This technique enables a side-by-side comparison of diffusion and viscous relaxation. The reduction in mass diffusivity is attributed

both to side-group association and to molecular weight effects. Future FRAP studies on monodisperse polymers are needed to properly isolate each effect. Arrhenius plots of molecular diffusivity and shear viscosity indicate that H-bond association of side-groups affects diffusion and viscous relaxation in fundamentally different ways. Small molecule diffusion through UPy-containing PBA appears to be limited more by thermal equilibrium, *i.e.* the value of the association constant K . On the other hand, viscous relaxation is limited by the frequency of H-bonding dissociation, *i.e.* the value of the rate constant k_d .

Acknowledgements

The authors acknowledge support from funding provided by the National Science Foundation under Grant DMR-0906627. J.L. appreciates support from a Horton Fellowship administered through Laboratory of Laser Energetics. E.B. appreciates support from Era of Hope Scholar Award W81XWH-05-1-0396.

Notes and references

- 1 G. Broze, R. Jerome and P. Teyssié, *Macromolecules*, 1981, **14**, 224–225.
- 2 R. P. Sijbesma, F. H. Beijer, L. Brunsved, B. J. B. Folmer, J. H. K. K. Hirschberg, R. F. M. Lange, J. K. L. Lowe and E. W. Meijer, *Science*, 1997, **278**, 1601–1604.
- 3 J. Li, J. A. Viveros, M. H. Wrue and M. Anthamatten, *Adv. Mater.*, 2007, **19**, 2851–2855.
- 4 K. Yamauchi, J. R. Lizotte and T. E. Long, *Macromolecules*, 2003, **36**, 1083–1088.
- 5 P. Cordier, F. Tournilhac, C. Soulie-Ziakovic and L. Leibler, *Nature*, 2008, **451**, 977–980.
- 6 L. Leibler, M. Rubinstein and R. H. Colby, *Macromolecules*, 1991, **24**, 4701–4707.
- 7 S. Sivakova, D. A. Bohnsack, M. E. Mackay, P. Suwanmala and S. J. Rowan, *J. Am. Chem. Soc.*, 2005, **127**, 18202–18211.
- 8 M. J. Serpe, M. Rivera, F. R. Kersey, R. L. Clark and S. L. Craig, *Langmuir*, 2008, **24**, 4738–4742.
- 9 W. C. Yount, D. M. Loveless and S. L. Craig, *Angew. Chem., Int. Ed.*, 2005, **44**, 2746–2748.
- 10 S. H. M. Soentjens, R. P. Sijbesma, M. H. P. van Genderen and E. W. Meijer, *J. Am. Chem. Soc.*, 2000, **122**, 7487–7495.
- 11 A. Zosel and G. Ley, *Macromolecules*, 1993, **26**, 2222–2227.
- 12 K. C. Tseng, N. J. Turro and C. J. Durning, *Polymer*, 2000, **41**, 4751–4755.
- 13 Y. Cheng, R. K. Prud'homme and J. L. Thomas, *Macromolecules*, 2002, **35**, 8111–8121.
- 14 E. Van Keuren and W. Schrof, *Macromolecules*, 2003, **36**, 5002–5007.
- 15 E. B. Brown, E. S. Wu, W. Zipfel and W. W. Webb, *Biophys. J.*, 1999, **77**, 2837–2849.
- 16 J. S. Vrentas and C. M. Vrentas, *J. Appl. Polym. Sci.*, 1991, **42**, 1931–1937.
- 17 M. Rubinstein and A. N. Semenov, *Macromolecules*, 1998, **31**, 1386–1397.
- 18 D. J. M. van Beek, A. J. H. Spiering, G. W. M. Peters, K. te Nijenhuis and R. P. Sijbesma, *Macromolecules*, 2007, **40**, 8464–8475.
- 19 J. Sprakel, J. van der Gucht, M. A. C. Stuart and N. A. M. Besseling, *Phys. Rev. E*, 2008, **77**, 061502.
- 20 J. van der Gucht, N. A. M. Besseling, W. Knoben, L. Bouteiller and M. A. C. Stuart, *Phys. Rev. E*, 2003, **67**, 051106.

Measurement of the ratio of forward-propagating to back-propagating second harmonic signal using a single objective

Xiaoxing Han¹ and Edward Brown^{2,*}

¹*Institute of Optics, University of Rochester, Goergen Hall Box 270168, Rochester, New York 14627, USA*

²*Department of Biomedical Engineering, University of Rochester, Goergen Hall Box 270168, Rochester, New York 14627, USA*

**Edward_Brown@urmc.rochester.edu*

Abstract: In this paper, we present a method to determine, for the first time, the ratio of forward-propagating second harmonic (SHG) signal to back-propagating SHG signal (F/B) in vivo on the surface of intact tissue samples without any biopsy or tissue sectioning, using only epidetection (i.e., via a single objective lens). This method has the additional benefit of using the confocal detection apparatus already contained within common commercially available two-photon laser-scanning microscopes, and hence can allow the measurement of the SHG F/B ratio in vivo with minimal purchase of new equipment.

© 2010 Optical Society of America

OCIS codes: (170.0170) Medical Optics and Biotechnology; (180.0180) Microscopy

References and links

1. R. M. Williams, W. R. Zipfel, and W. W. Webb, "Interpreting second-harmonic generation images of collagen I fibrils," *Biophys. J.* **88**(2), 1377–1386 (2005).
2. R. LaComb, O. Nadiarnykh, and P. J. Campagnola, "Quantitative second harmonic generation imaging of the diseased state osteogenesis imperfecta: experiment and simulation," *Biophys. J.* **94**(11), 4504–4514 (2008).
3. O. Nadiarnykh, R. B. LaComb, P. J. Campagnola, and W. A. Mohler, "Coherent and incoherent SHG in fibrillar cellulose matrices," *Opt. Express* **15**(6), 3348–3360 (2007).
4. X. Han, R. M. Burke, M. L. Zettel, P. Tang, and E. B. Brown, "Second harmonic properties of tumor collagen: determining the structural relationship between reactive stroma and healthy stroma," *Opt. Express* **16**(3), 1846–1859 (2008).
5. A. C. Kwan, D. A. Dombeck, and W. W. Webb, "Polarized microtubule arrays in apical dendrites and axons," *Proc. Natl. Acad. Sci. U.S.A.* **105**(32), 11370–11375 (2008).
6. S. V. Plotnikov, A. C. Millard, P. J. Campagnola, and W. A. Mohler, "Characterization of the myosin-based source for second-harmonic generation from muscle sarcomeres," *Biophys. J.* **90**(2), 693–703 (2006).
7. O. Nadiarnykh, R. B. LaComb, M. A. Brewer, and P. J. Campagnola, "Alterations of the extracellular matrix in ovarian cancer studied by second harmonic generation imaging microscopy," *BMC Cancer* **10**(1), 94 (2010).
8. F. Légaré, C. Pfeffer, and B. R. Olsen, "The role of backscattering in SHG tissue imaging," *Biophys. J.* **93**(4), 1312–1320 (2007).
9. L. Wang, and S. L. Jacques, "Hybrid model of Monte Carlo simulation and diffusion theory for light reflectance by turbid media," *J. Opt. Soc. Am. A* **10**(8), 1746–1752 (1993).
10. W. F. Cheong, S. A. Prahl, and A. J. Welch, "A review of the optical properties of biological tissues," *IEEE J. Quantum Electron.* **26**(12), 2166–2185 (1990).
11. T. J. Farrell, M. S. Patterson, and B. Wilson, "A diffusion theory model of spatially resolved, steady-state diffuse reflectance for the noninvasive determination of tissue optical properties in vivo," *Med. Phys.* **19**(4), 879–888 (1992).
12. W. R. Zipfel, R. M. Williams, and W. W. Webb, "Nonlinear magic: multiphoton microscopy in the biosciences," *Nat. Biotechnol.* **21**(11), 1369–1377 (2003).

1. Introduction

Recently, second harmonic generation (SHG) has proven to be a useful window into the amount and organization of fibrillar collagen in biological tissues due to its relative specificity and the fact that it is an intrinsic signal [1–6]. SHG is a coherent phenomenon, which implies that SHG is sensitive not only to the amplitude of the illumination field but also to its phase. In addition to a spatial resolution that is equal to other imaging techniques

(such as two photon excited fluorescence), SHG microscopy can provide information about the sample's molecular structure. For example, the ratio of the forward-propagating to backward propagating SHG signal (the "F/B ratio") can help us to understand the axial extent of ordering in collagen fibers [1–5].

Previously, *in vitro* measurements of SHG F/B ratios have been used to study collagen fiber ordering in various tissue samples such as rat tail, ovarian cancer biopsies, mouse models of breast cancer, and dermis from mouse models of Osteogenesis Imperfecta (OIM) [1–5,7]. The F/B ratio revealed the length scale of ordering in the fibers and in the case of OIM and ovarian cancer, was able to discriminate pathological tissue from healthy tissue [2,7]. In these measurements a second objective lens was needed to collect forward propagating SHG signal. Hence, the tissue sample had to be dissected from the animal and sectioned to 100 μ m slices to allow signal to reach the second detection lens. For clinical application, such as in endoscopy, it is impossible to put an objective and a PMT detector underneath the tissue sample to collect the forward propagating SHG. The excision and sectioning required to use a second detector for forward propagating SHG also prevents dynamic measurements of collagen ordering over time. Therefore, it becomes highly desirable to develop a new optical system to measure collagen SHG F/B ratio *in vivo*, using only epi-detection and on intact thick tissue samples.

2. Experimental methods

2.1 Optical setup

The optical setup we are using to determine the SHG F/B ratio *in vivo* using only epidetection is shown in Fig. 1 below. SHG signal was generated by a Spectra Physics MaiTai Ti:Sapphire laser providing 100fs pulses at 80 MHz and 810 nm. The excitation beam was directed into an Olympus Fluoview F300 scanhead connected to an Olympus BX61WI upright microscope. The focusing objective is an Olympus UMPLFL20XW water immersion lenses (20 \times , 0.5 N.A.), with supporting measurements performed using an Olympus LUMPlanFL/IR (40x, 0.8 NA) water immersion lens. This objective was used to focus the excitation beam on the sample and at the same time collect the direct backward-propagating SHG as well as the forward-propagating SHG signal that was subsequently backscattered within the tissue. The SHG signal was collected by the objective, converged by the tube lens, and collimated by the pupil lens. The collimated SHG beam was then de-scanned and focused again on the pinhole plane by the collector lens. All of these lenses are intrinsic to the BX61WI microscope or the Fluoview F300 scanhead. The focal lengths of the pupil lens and the collector lens are 54mm and 185mm respectively, and size of the pinholes on the F300 variable pinhole turret are 60 μ m, 100 μ m, 150 μ m, 200 μ m and 7000 μ m. The SHG beam was separated from the excitation beam by a dichroic mirror (Chroma 670 DCSX) inserted into the F300 scanhead, as well as a band pass filter centered at 405 nm (Chroma HQ405/30m-2P) placed after the pinhole, and detected by the FV300's intrinsic photomultiplier tubes. The only significant equipment modifications are insertion of the aforementioned dichroic mirror and filter in the appropriate location in the scanhead, and the punching out of one of the pinholes in the pinhole turret to produce one extremely large pinhole setting (see below).

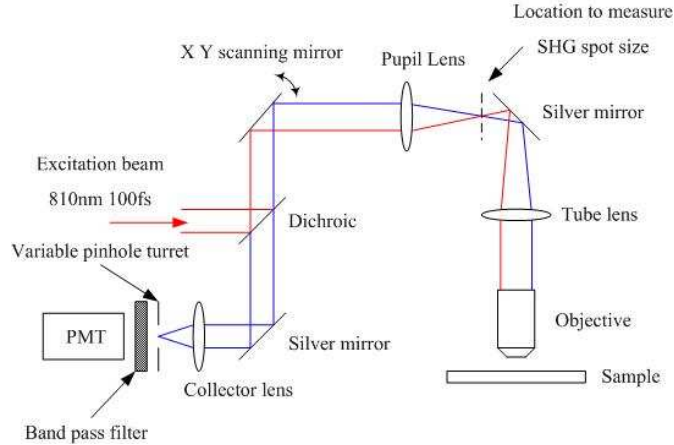


Fig. 1. Experimental setup for in vivo measurement of tumor collagen SHG F/B ratio.

2.2 SHG Back Scattering and Monte Carlo Simulation

Using the apparatus described above, we generate an SHG image using confocal detection of the resultant SHG. While much of the forward-propagating SHG signal will travel into the tissue sample and be lost to our objective lens, a fraction of this signal undergoes multiple scattering events and passes back through the object plane, traveling towards the objective lens. As shown in Fig. 2, this signal will pass through the object plane at multiple locations. Conversely, at shallow imaging depths the backwards-propagating SHG signal will emanate from the image plane only from the two-photon focal volume with minimal subsequent scatter. When the object plane is imaged onto the confocal pinhole, the spatial distribution of SHG signal on the confocal plane will consist of a sharp central peak due to the backward propagating SHG plus a diffuse signal due to the forwards propagating and subsequently backscattered SHG. As discussed below, our new method consists of repeatedly imaging the sample through a series of different sized pinholes, whereby the shape of this total SHG distribution can be measured and, with suitable calibration, the underlying F/B ratio can be determined.

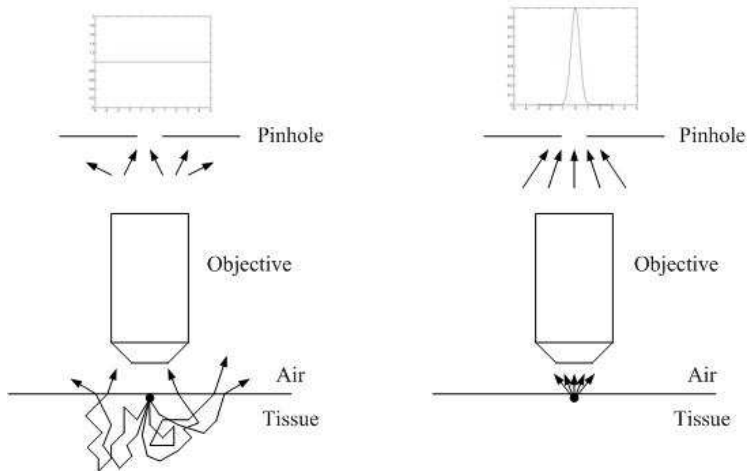


Fig. 2. Back scattering of forward-propagating SHG and propagation of direct backward propagating SHG

In order to implement this method we must first understand the spatial distribution, in the object plane, of forward propagated light that subsequently backscatters and reaches that

plane. 405 nm SHG signal is easily scattered while propagating in the tissue sample. In Legare et al 2007 [8], it was determined that ~21% of the forward-propagating SHG signal was subsequently backscattered and reached the tissue surface, and that the epi-detected image from a 5mm thick Achilles tendon tissue block was actually a combination of the direct backward propagating SHG signal and the forward propagating SHG signal that was subsequently backscattered. In fact for collagen fibers in some tissue samples, such as in mouse breast tumor models, the SHG F/B ratio is very high (~30) [4], and most SHG signal propagates in the forward direction. In these cases epi-detected SHG microscopy is greatly enhanced due to the subsequent backscattering of the forward propagating SHG.

The propagation of light in turbid media can be well modeled by Monte Carlo simulation of the paths that photons make as they travel through tissue, which are chosen by statistically sampling the probability distributions for step size and angular deflection per scattering event. Using a Monte Carlo code based closely upon that of Wang et al [9] (see Appendix), we sent 405nm SHG photons into an infinitely deep scattering tissue in the forward direction. The SHG photons were emitted from a point source and we ignored the direct backward propagating SHG photons. We experimentally measured the angular distribution of the forward propagating SHG emission by imaging the back focal plane of an objective lens which was collecting the forward propagating SHG from a 100 μm section of tumor tissue, and found that the forward SHG from collagen fibers is emitted in a rather tight beam confined to ± 15 degrees around the laser axis (data not shown). Hence we used the same initial angular distribution (± 15 degrees around the axis normal to the tissue-air surface) in the Monte Carlo simulation. The scattering particles are modeled as 10 μm diameter cells, the refractive indexes inside and outside of the cells are 1.38 and 1.42 respectively, and the scattering and absorption coefficients we used in the simulation are $\mu_a = 0.7 \text{ cm}^{-1}$ and $\mu_s = 150 \text{ cm}^{-1}$ [10]. The probability distribution of scattering angles after every scattering event were calculated according to Mie theory with the cell size and the refractive index inside and outside of the cells, with a 99% chance the scattering angle will fall between ± 6 degrees. We then counted the number of photons which escape from the air-tissue surface in the backward direction and plotted out the steady state distribution of the backscattered photons over the radial distance from the emission point.

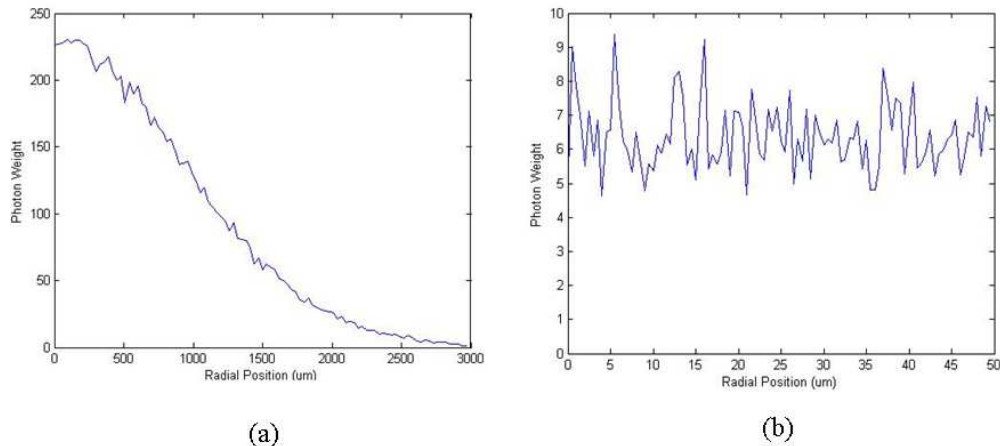


Fig. 3. Monte Carlo simulation of forward propagating and subsequently backscattered SHG photons which reach the object plane.(a) Steady state radial distribution of the backscattered SHG photons over a large range of radial position (3mm) (b) The same distribution over a short radial range (50 μm)

The simulation results are shown in Fig. 3. Figure 3(a) shows the steady state distribution of the forward propagating and subsequently backscattered SHG photons which reach the object plane, over a large range of radial positions i.e. from the center to 3mm away from the

emission point. Figure 3(b) shows the same distribution over a short range i.e. from the center to only 50um away from the emission point, which is the length scale of our largest pinhole setting (where the pinhole-bearing foil has been punched out). We can see from Fig. 3(a) that over a large length scale the forward propagating and subsequently back-scattered SHG photon intensity decays exponentially with the distance from emission point, which agrees with previous literature [11]. But from Fig. 3(b) we can see over a very short range of 50 um, the range covered by our pinhole settings and where the diffusion approximation does not hold [11], the intensity of forward propagating and subsequently back scattered SHG photons is constant and does not depend on distance from the focal volume.

2.3 Fitting model

To measure collagen fiber SHG F/B ratio *in vivo* with only the epi-detection objective, we will generate a series of collagen fiber SHG images, in the backward channel, through a series of confocal pinholes of different sizes which correspond to a diameter in the object plane ranging from 0.874 um to 102 um (see 3.1 below). As discussed above, the SHG signal we collect after the pinhole is a mixture of both the direct backward propagating SHG and the forward propagating and subsequently backscattered SHG. To analyze our experimental data we model the image in the pinhole plane of the direct backward propagating SHG signal plane as a Gaussian spot [12], while the forward propagating SHG that subsequently backscatters is modeled as a uniform distribution over these length scales (based upon the results of our Monte Carlo simulation, as described above). So the total SHG signal intensity distribution on the object plane can be expressed as:

$$I_{SHG}(r) = B \exp[-2(\frac{r}{\omega})^2] + FC, \quad (1)$$

where ω is the e-2 Gaussian spot size of the direct backward propagating SHG, F and B are absolute intensities of forward and backward propagating SHG signals, the parameter C relates the initial forward propagating signal intensity to the average intensity of the uniform distribution of SHG light that reaches the object plane, and is a function of scattering and absorption properties of the underlying tissue. Alternatively, this expression can be written in another way,

$$I_{SHG}(r) = B[\exp[-2(\frac{r}{\omega})^2] + \frac{F}{B}C], \quad (2)$$

where F/B represents the collagen fiber SHG F/B ratio.

When we generate collagen fiber SHG images through a series of confocal pinholes of different sizes, each pixel on that image represents an integration of the total SHG signal over the pinhole area

$$I_{pixel} \propto \int_0^{2\pi} d\theta \int_0^R \left\{ \exp[-2(\frac{r}{\omega})^2] + \left(\frac{F}{B}\right)C \right\} r dr, \quad (3)$$

where R is the size of the pinhole with respect to Gaussian spot size of the direct backward propagating SHG, i.e. $R = r_{pinhole}/\omega$. If the pixel intensities at various pinhole sizes are normalized to the maximum pixel intensity at the largest pinhole size, the relative pixel intensity is a function of relative pinhole size R:

$$I_{rel}(R) = \frac{\int_0^{2\pi} d\theta \int_0^R \left\{ \exp[-2(\frac{r}{\omega})^2] + \left(\frac{F}{B}\right)C \right\} r dr}{\int_0^{2\pi} d\theta \int_0^{R_{max}} \left\{ \exp[-2(\frac{r}{\omega})^2] + \left(\frac{F}{B}\right)C \right\} r dr}, \quad (4)$$

where R_{max} is the largest pinhole size in our system. With this expression we can plot the relative pixel intensity versus pinhole size and fit the data to produce $(F/B)C$. In order to determine F/B we must then eliminate C , the fraction of signal which originally propagates in the forward direction but is eventually backscattered by the tissue and reaches the pinhole plane. This can be done by introducing into the sample a reference of known F/B ratio, whose C value is the same. In these experiments we used blue fluorescent polystyrene beads (peak $\lambda_{em} = 424\text{nm}$) sprinkled onto the sample surface. The quantity $(F/B)C$ is then determined for both the calibration beads in the image, as well as the fibers of interest. Next, the correction factor that is required to convert the measured values of bead $(F/B)C$ to the known value of F/B is determined, and the previously unknown value of fiber F/B is determined from the measured $(F/B)C$ using the same correction factor:

$$\frac{\text{measured collagen SHG } F/B \text{ Ratio}}{\text{measured beads TPEF } F/B \text{ Ratio}} = \frac{\text{real collagen SHG } F/B \text{ Ratio}}{\text{real beads TPEF } F/B \text{ Ratio}}. \quad (5)$$

To illustrate the fitting function given by Eq. (4) in the case of the typical backscattering fraction $C = 0.001$ and $R_{max} = 28$ we can plot out the relative pixel intensity v.s. pinhole size curves at various collagen fiber SHG F/B ratios in Fig. 4:

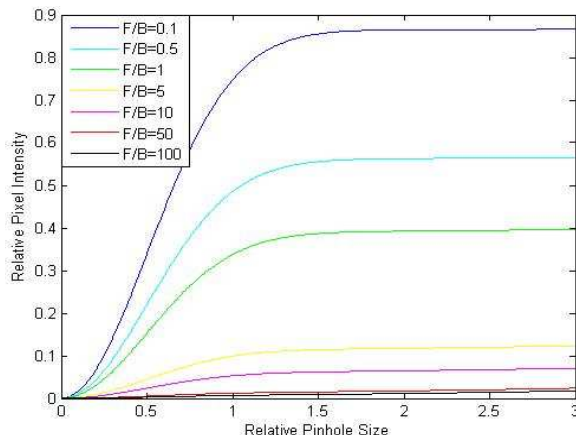


Fig. 4. Relative SHG intensity vs. relative pinhole size curves at different collagen SHG F/B ratios, based upon Eq. (4). The relative SHG intensities equal 1 at a pinhole size of $r = R_{max} = 28$.

From this plot one can see the sharp curvature due to the Gaussian distribution of direct back-propagating SHG (most evident in the steep early rise of the curves with small values of F/B) and the slow and steady rise due to forward-propagating light that is subsequently backscattered and produces a diffuse signal which does not vary with r (most evident in the slow rise of the curves with large values of F/B). This reveals the utility in punching out one of the metal foils containing a pinhole from the pinhole turret of the scanner, as this produces one pinhole of extremely large size ($R = 28$ in the case of the Fluoview 300) whose radius is far from the initial sharp curvature due to the Gaussian distribution of direct back-propagating SHG, allowing the collection of a great deal of the diffuse forward-propagated signal.

3. Results

3.1 Determining backward propagating SHG spot size on the pinhole plane

In order to produce the required plot of SHG signal versus pinhole size and fit it with our model, we must first determine the sizes of the pinholes, relative to the Gaussian spot size of the direct backward propagating SHG on the pinhole plane. Since we are determining the spot size in the pinhole plane of the direct backward propagating SHG, we must avoid significant backscattering of the forward propagating SHG. Therefore rat tail collagen samples were fresh frozen and sectioned into 10um thin slices, spread out on a cover slip and dried

overnight in a refrigerator for good adhesion between sample sections and cover slip. The cover slip was then flipped over with the sample side facing down, submerged in PBS and the excitation beam transmitted through the cover slip. The sample was submerged in saline to minimize the refractive index change and thus reduce the subsequent backscattering of the forward propagating SHG. The saline container is a cup with 4 cm diameter and 4 cm depth. It was painted black to absorb forward propagating SHG that goes through the sample section (see Fig. 5).

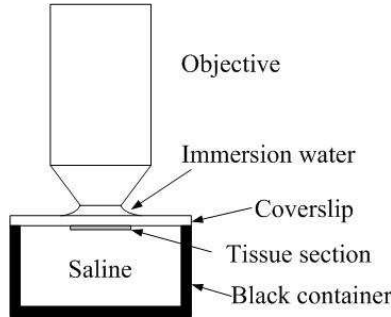


Fig. 5. Configuration of objective, sample and scatterer holder

To determine the size of the image of the SHG spot in the pinhole plane, we measured the SHG spot directly with a CCD camera (SPOT RT3, SciTech) at the intermediate image plane depicted on Fig. 1. The SHG spot in the pinhole plane is just a magnified version of the spot we captured with the CCD camera with a magnification factor of the ratio of the focal length of the pupil lens and collection lens.

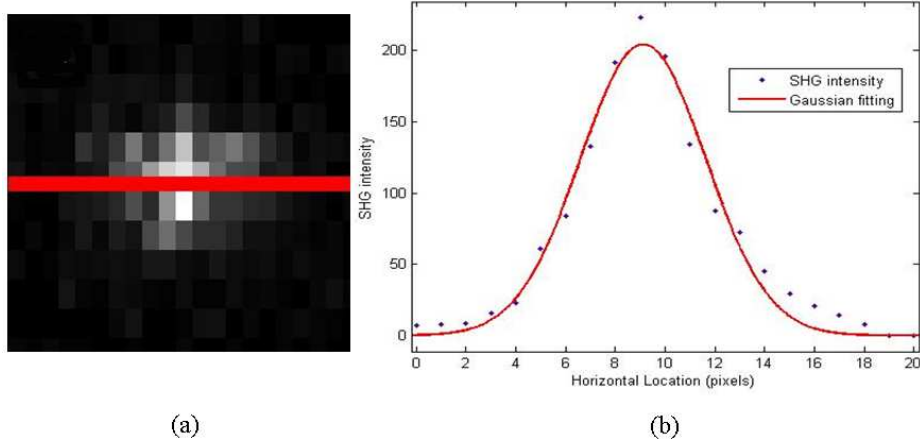


Fig. 6. Determination of SHG spot size. (a) CCD captured image of SHG focal spot after the tube lens (b) SHG intensity along the straight line that goes through the center of SHG spot. The red straight line in (a) is the line along which SHG intensities are measured. The red curve in (b) is the Gaussian fit to the intensities we measured in (a)

As shown in Fig. 6(a) above, we drew a straight line through the center of the SHG spot captured by CCD camera, and measured SHG intensity along this line. The SHG intensity vs. horizontal location data set was then plotted in Fig. 6(b) as a series of separate points, and fitted to a Gaussian model producing an average spot size in the intermediate image plane of 9.34 pixels or 69 μm . Taking into account the magnification factor of the pupil and collector lens, the average pinhole plane spot size of the backward propagating SHG is therefore 236.8 μm . We already knew the absolute diameters of the five pinholes on the pinhole turret are 60 μm 100 μm 150 μm 200 μm to 7000 μm respectively (7000 μm corresponds to the location in the pinhole turret where we punched out the pinhole-bearing metal foil). That corresponds to

0.24 ω , 0.4 ω , 0.6 ω , 0.8 ω and 28 ω , where ω stands for the e-2 SHG spot size in the pinhole plane.

3.2 Measurement of SHG intensity varied with pinhole size

To evaluate our new method we chose the rat tail tendon, a sample whose SHG properties have been well studied [1]. A whole rat tail was removed from a previously sacrificed animal (removal from the animal is not necessary for the technique but is convenient for handling the sample). To generate a clear SHG image of the tendon in particular (to match the sample previously studied in the literature) we peeled a thin layer of outer skin off the rat tail at the location of interest and exposed the tendon beneath it. We then put the rat tail on a glass slide, with the exposed collagen fiber facing up and we put another coverslip on top of the collagen fibers to ensure a stable sample. The rat tail and coverslip were then fixed on the glass slide with plastic tape and the collagen fibers were imaged through the coverslip. Note that, unlike previous methods which measure F/B with a second detector for the forward-propagating SHG, the tendons remained within the ~1cm diameter tail.

We prepared whole rat tail samples from 5 separate animals (see Fig. 7). On each rat tail we chose 5 image fields. And for each image field we took 5 back detected SHG images with the pinhole size varied from 60um 100um 150um 200um to 7000um, plus one image with no sample in order to quantify the background noise. One of these image sets is shown below.

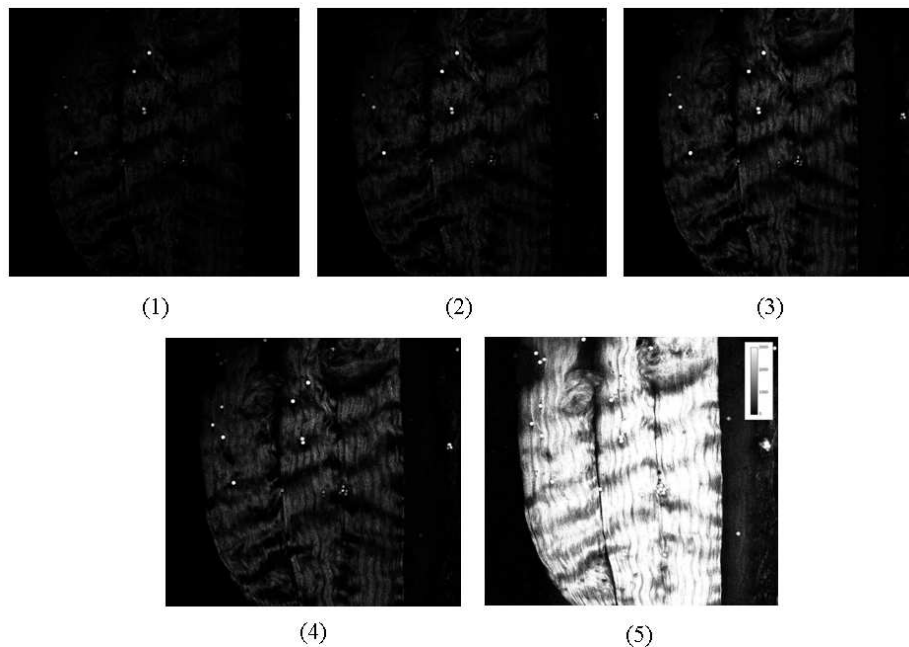


Fig. 7. In vivo SHG images of rat tail collagen fibers in an intact rat tail. Images 1-5 are SHG images of the same ROI when the size of the pinhole varied from 60um, 100um, 150um, 200um, to 7000um, respectively. The bright spots are blue fluorescent polystyrene beads for calibration. Images are 600 um across.

3.3 Curve fitting and prediction of collagen SHG F/B ratio

In each set of images, we picked 5 small regions of interest (ROIs) around collagen fibers and 3 regions of interest around the calibration beads. ROIs were drawn around fibers that extended over at least ~100 um in the image plane, to ensure that fibers were close to perpendicular to the optical axis. A length 100 um in an optical section of ~12 um thickness (e-2 z diameter of the PSF) corresponds to a maximum angle in the object plane of ~7 degrees. Signal intensities in these collagen and beads ROIs were measured with ImageJ,

background was subtracted, and signal intensities were normalized so that the maximum intensity measured with the largest pinhole was set to 1. The average relative SHG intensity of all 25 collagen ROIs (5 ROIs in each of 5 image stacks) and average relative TPEF intensity of all 15 beads ROIs in one rat tail vs. relative pinhole size plot is shown below. Note the separation between the collagen fiber curve and the bead curve due to the different F/B ratios of rat tail collagen and fluorescent calibration beads.

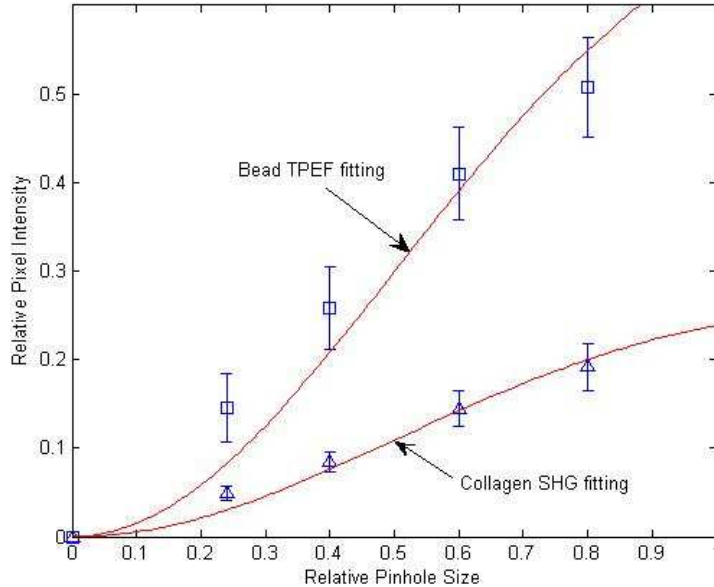


Fig. 8. Epidetected total collagen SHG intensity (blue triangles), or total bead TPEF intensity (blue squares) vs. pinhole size, fit to the model given by Eq. (4) (red lines). The horizontal axis is pinhole size in units of backward propagating SHG spot size on the pinhole plane i.e. fraction of ω . The vertical axis is normalized SHG intensity. Note that the fitting curves identically equal 1 when the pinhole size reaches $R = 28$, whose data point is not shown, and that the intensity information for $R = 28$ provides the normalization value and hence is included in the overall fit.

As described above, for one rat tail we measured relative intensity in 25 collagen ROIs and 15 bead ROIs. For each ROI 5 relative intensities were measured with size of the pinhole varying from the smallest to the largest. Average relative SHG intensity of all 25 collagen ROIs and average relative TPEF intensity of all 15 bead ROIs, as shown in Fig. 8, were considered a set of data for one rat tail. We then fit this set of real measured data to the model given in Eq. (4) and calculated the rat tail collagen fiber SHG F/B ratio in one animal by eliminating C using Eq. (5). This data collection/averaging/curve fitting/calculation process was repeated 5 times to calculate rat tail collagen fiber SHG F/B ratio in 5 animals. The results are listed in Table 1 below.

Table 1. Results of in vivo measured rat tail collagen SHG F/B ratio

	Animal I	Animal II	Animal III	Animal IV	Animal V	Average
F/B ratio	2.10 ± 0.19	1.81 ± 0.30	2.50 ± 0.34	1.34 ± 0.13	2.26 ± 0.23	2.00 ± 0.45

For each animal, means \pm 95% confidence intervals are presented, with the data from 25 ROIs being pooled to produce a single curve fit for each animal. The average value for the 5 animals is then presented \pm the standard deviation.

To verify the validity of our method using thick samples and only epi-detection, we also directly measured rat tail collagen SHG F/B ratio with both forward and backward detectors and with the sample sectioned in $\sim 10\text{ }\mu\text{m}$ thin slices, as previously described [4]. In summary,

the SHG image captured in the forward detector was divided by the SHG image captured in the backward detector. We then averaged SHG F/B ratio over all pixels within collagen fibers and ignored all pixels outside the collagen fibers. The scattering of the tissue, though very low in this case, was corrected for by measuring the F/B ratio of the TPEF signals from 10 μ m diameter calibration fluorescent beads.

The measurement results from 5 animals, using forward and backwards detectors, are listed in Table 2.

Table 2. Results of in vitro measured rat tail collagen SHG F/B ratio

	Animal VI	Animal VII	Animal VIII	Animal IX	Animal X	Average
F/B ratio	1.43 \pm 0.80	1.22 \pm 0.27	2.29 \pm 0.49	1.75 \pm 0.50	2.11 \pm 0.86	1.76 \pm 0.45

For each animal, means \pm standard deviations are presented from 5 F/B measurements. The average value for the 5 animals is then presented \pm the standard deviation.

The overall average F/B ratio from 5 animals is 1.76 \pm 0.45. This result was not statistically significantly different from our measurement using only the epi-detection objective lens and the model given by Eq. (4) (Student's t-test $p = 0.42$) demonstrating that the results from the two methods are in good agreement. To evaluate the new method at a higher NA we also measured the F/B ratio using a 0.8 NA lens, producing a value for F/B (1.37 \pm 0.28) which is again not statistically significantly different from the direct measurement using forward and backwards detectors ($p = 0.17$ $N = 5$).

4. Discussion

In this paper, we present a method to measure the SHG F/B ratio with only an epi-detection objective lens, allowing measurement on thick tissue samples. In our demonstration we used the whole rat tail (\sim 1 cm thick), with the rat removed for convenience, but the technique is equally applicable to a live specimen. By obviating the need for thin sectioning of the sample, this technique provides the opportunity to do time-dependent studies, as well as the possibility of use in an endoscopic setting. This is significant because SHG F/B ratios have been shown to be of interest in discriminating skin with Osteogenesis Imperfecta [2] from normal dermis [2] and SHG F/B ratio measurements have been used to help determine the organization of fibrillar collagen in samples such as breast tumor models [4], in rat tail tendon [1], cellulose [3], mouse Achilles tendon [8], muscle fascia [8], and ovarian cancer [7] (although see 4.2 Limitations, below). Furthermore, the confocal pinholes used in this technique are available in most commercial two photon microscopes, allowing the measurement of the SHG F/B ratio in intact specimens without addition of new equipment (assuming one is already using a two-photon microscope to study SHG) or extensive equipment modification (except for a single dichroic and filter inserted in the dichroic holder of the scanbox, and the punching out of one of the pinhole settings to produce one very large pinhole).

4.1 Sensitivity

In order to determine the radial intensity distribution of the forward propagating and subsequently backscattered SHG using a Monte Carlo simulation, the tissue scattering parameters we used in the simulation were $\mu_a = 0.7 \text{ cm}^{-1}$ and $\mu_s = 150 \text{ cm}^{-1}$, which are typical values for 405 nm light [10]. However, the scattering properties of tissue vary over a large range among different organs throughout the body, and it is reasonable to wonder if this fitting model is good for all types of tissues from different organs. To determine this we varied the scattering parameters over a large range and repeated the Monte Carlo simulation with the results shown in Fig. 9 and Fig. 10.

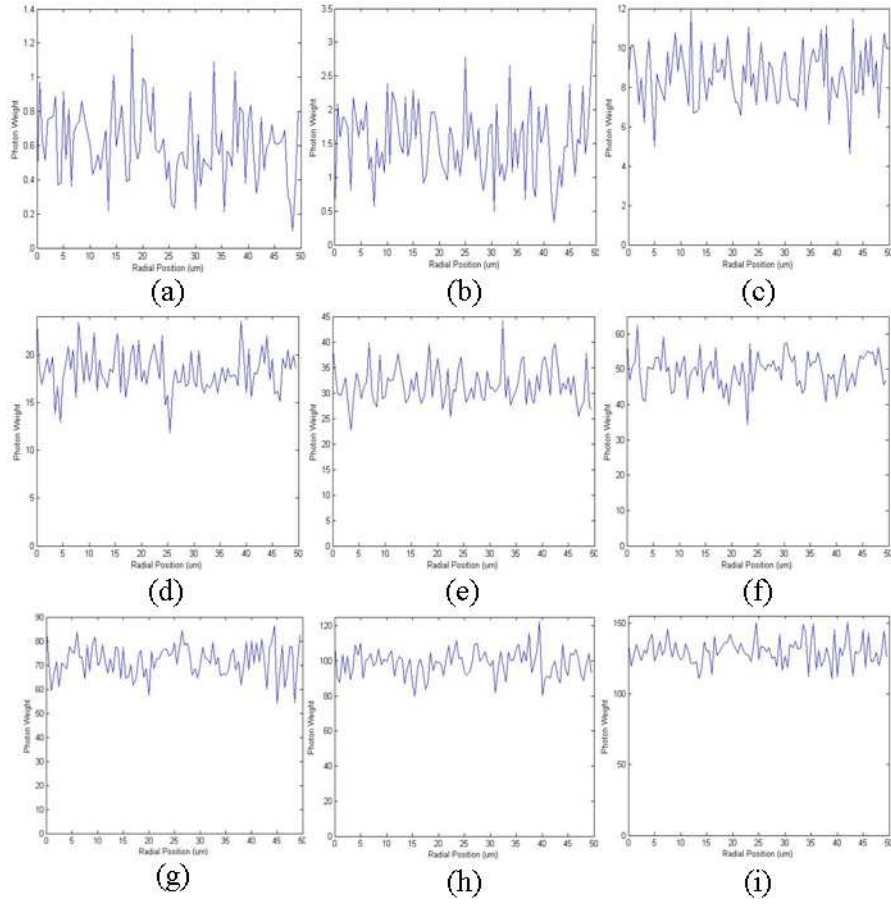


Fig. 9. Monte Carlo simulation of forward propagating SHG that is subsequently backscattered and reaches the object plane, with varying μ_s . Steady state radial distribution of the backscattered SHG photons when (a) $\mu_s = 100 \text{ cm}^{-1}$ (b) $\mu_s = 150 \text{ cm}^{-1}$ (c) $\mu_s = 200 \text{ cm}^{-1}$ (d) $\mu_s = 250 \text{ cm}^{-1}$ (e) $\mu_s = 300 \text{ cm}^{-1}$ (f) $\mu_s = 350 \text{ cm}^{-1}$ (g) $\mu_s = 400 \text{ cm}^{-1}$ (h) $\mu_s = 450 \text{ cm}^{-1}$ (i) $\mu_s = 500 \text{ cm}^{-1}$. In each case $\mu_a = 0.7 \text{ cm}^{-1}$

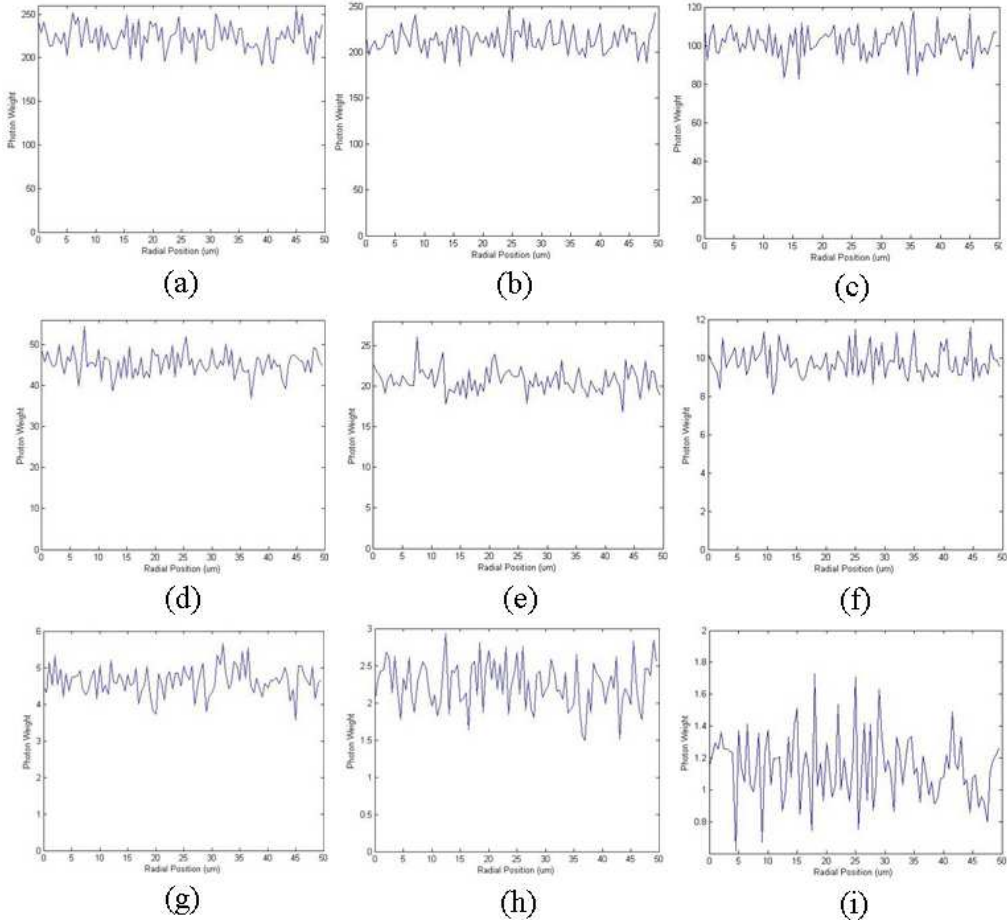


Fig. 10. Monte Carlo simulation of forward propagating SHG that is subsequently backscattered and reaches the object plane, with varying μ_a . (a) Steady state radial distribution of the backscattered SHG photons when (a) $\mu_a = 0.05 \text{ cm}^{-1}$ (b) $\mu_a = 0.1 \text{ cm}^{-1}$ (c) $\mu_a = 1 \text{ cm}^{-1}$ (d) $\mu_a = 2 \text{ cm}^{-1}$ (e) $\mu_a = 3 \text{ cm}^{-1}$ (f) $\mu_a = 4 \text{ cm}^{-1}$ (g) $\mu_a = 5 \text{ cm}^{-1}$ (h) $\mu_a = 6 \text{ cm}^{-1}$ (i) $\mu_a = 7 \text{ cm}^{-1}$. In all three cases $\mu_s = 500 \text{ cm}^{-1}$

We can see from the simulation results that when μ_a decreases or μ_s increases more forward propagating SHG photons reach the object plane after subsequent backscattering; and when μ_a increases or μ_s decreases less reach the object plane. However, over a range of scattering parameters in our Monte Carlo simulations that are comparable to values found at these wavelengths in the literature [10], varying μ_a and μ_s does not alter the distribution of light exiting the tissue over the 0-50 μm length scale, and it remains a constant, independent of radial position (a slope of zero is within the 95% confidence interval). We therefore conclude that within this small region of the object plane close to the optical axis, which is the region covered by our pinhole distribution, the radial intensity distribution of the backscattered SHG is not affected by a wide variety of tissue scattering parameters, and this fitting model is therefore applicable for tissue from diverse organs.

4.2 Limitations

This technique has two significant limitations. As shown in Fig. 4, when the F/B ratio increases, the separation between two SHG intensity vs. pinhole size curves decreases. Using a reasonable value for C [8], Fig. 4 shows that when the collagen fiber SHG F/B ratio is significantly more than ~ 5 , the two curves are so close that they are not likely to be

distinguishable assuming typical variation in experimental data (such as shown in Fig. 8). This implies that the new method might not be applicable for samples with collagen fiber SHG F/B ratios significantly higher than ~ 5 . To illustrate this, we applied this method to measure the SHG F/B ratio of collagen fibers in intact mouse skeletal muscle fascia (with overlying skin removed to allow access). Using the new technique, we produced a value of the collagen fiber F/B ratio *in vivo* of 5.05 ± 0.81 ($N = 5$) while after extracting the fascia, mounting it between two coverslips and directly measuring SHG F/B ratio with two objective lenses we produced a value of 5.56 ± 1.03 ($N = 5$), which was not statistically significantly different ($p = 0.43$). We also applied this method to measure the SHG F/B ratio of collagen fibers in 4T1 breast tumor models. According to our previous work the true collagen fiber SHG F/B ratio in 4T1 mouse breast tumor is ~ 30 . We measured collagen fiber SHG F/B ratio *in vivo* in whole tumor samples from 5 different animals (25 ROIs per animal), and the result is 6.64 ± 2.98 (data not shown). As predicted, as the F/B becomes significantly larger than ~ 5 , the result becomes inaccurate and noisy, with a greater relative standard deviation, because of the normal random noise in the experimental data combined with the insensitivity of this new technique to large F/B values. Fortunately, our data and published studies reveal that the F/B ratio in many biological samples is at or below five, including in the rat tail tendon (F/B~1), skeletal muscle fascia (F/B~5), cellulose (F/B~4), ovarian cancer (F/B ~ 3.4), and dermis with (F/B~3.4) and without (F/B~2.64) Osteogenesis Imperfecta [1–3,7,8]. Care must be taken when this technique produces F/B ratios significantly greater than five.

The second limitation arises from the fact that this technique assumes there is no subsequent scattering of back-propagating SHG signal. Hence it is limited to the surface, or extremely shallow imaging depths, of the sample and is suitable for quantifying F/B ratios on intact thick tissue samples, but not in intact thick tissue samples.

5. Conclusion

In this paper, we present a method to measure SHG F/B ratio suitable for intact tissue samples without sectioning, using just the epidetection objective lens. The method requires minor modification of the dichroics, filters, and confocal pinholes used in most commercial two photon microscopes and hence minimizes the purchase of new equipment. This allows F/B ratio measurements to be done in a dynamic fashion, and offers the possibility of endoscopic measurements. This technique is sensitive to F/B values up to ~ 5 and within this range are a variety of interesting and clinically relevant materials, tissues, and disease states, including tendon, fascia, cellulose, ovarian cancer, and dermis with and without Osteogenesis Imperfecta. The fact that OIM is within the range of this technique's sensitivity offers the attractive possibility of a non-invasive optical diagnosis of that disease, using a single objective lens, without biopsy samples being removed from the patient.

Acknowledgements

We thank Dr. Jerome Mertz for helpful conversations. This work is supported by a Department of Defense BCRP Pre-doctoral Traineeship Award (W81XWH-08-1-0323) to Xiaoxing Han, a Department of Defense BCRP Era of Hope Scholar Award (W81XWH05-1-0396), and a Pew Scholar in the Biomedical Sciences Award to Edward Brown III.